2006

Computational Study of Ring-Cusp Magnet Configurations that Provide Maximum Electron Confinement

Taiwo A. Ogunjobi
Wright State University

Computational Study of Ring-Cusp Magnet Configurations that Provide Maximum Electron Confinement

A thesis submitted in partial fulfillment
of the requirements for the degree of
Master of Science in Engineering

by

Taiwo A. Ogunjobi
Wright State University, 2004

2006
Wright State University

WRIGHT STATE UNIVERSITY

SCHOOL OF GRADUATE STUDIES

December 15, 2006

I HEREBY RECOMMEND THAT THE THESIS PREPARED UNDER MY SUPERVISION BY Taiwo A. Ogunjobi ENTITLED Computational Study of Ring-Cusp Magnet Configurations that Provide Maximum Electron Confinement BE ACCEPTED IN PARTIAL FULFILLMENT OF THE REQUIREMENTS FOR THE DEGREE OF Master of Science in Engineering.

James A. Menart, Ph.D.
Thesis Director

George P. Huang, Ph.D.
Department Chair

Committee on
Final Examination

James A. Menart, Ph.D.

Ravi C. Penmetsa, Ph.D.

Ruby P. Mawasha, Ph.D.

Joseph F. Thomas, Jr., Ph.D.
Dean, School of Graduate Studies

ABSTRACT

Taiwo Ogunjobi. M.S.Egr., Department of Mechanical and Materials Engineering, Wright State University, 2006. *Computational Study of Ring-Cusp Magnet Configurations that Provide Maximum Electron Confinement.*

Enhancing the confinement of primary electrons within the plasma in a discharge chamber of an ion thruster improves plasma ionization and consequently the thruster's performance. This work computationally calculates the location, position, and orientation of the permanent magnets that provide a ring-cusp magnetic field that maximizes electron confinement in an axi-symmetric cylindrical aluminum-wall discharge chamber. Small samarium cobalt magnets are circumferentially arranged in a ring around the front, side, or back wall of the chamber. The generated ring-cusp magnetic field for any specified magnet configuration is calculated using MAXWELL2D, a two dimensional electromagnetic field simulation computer code. For various magnet configurations, PRIMA, a particle-in-cell computer code modified by Mahalingam and Menart, is used to model the trajectory of the primary electrons in the magnetic field. The confinement length, the length of time an electron is retained within the chamber, is output by PRIMA, and it is the parameter used to determine the performance of the magnet configurations surveyed. The performance of various magnet ring pairs are studied and guidelines on the location, position, and orientation of the magnet rings are obtained. These guidelines are then combined to give complex ring-cusp magnet ring arrangements on a fixed size discharge chamber. For three complex arrangements having three magnet rings, a decrease in the chambers confinement ability is seen when the applied guidelines are slightly violated. This observed decrease validates the

guidelines deduced in this work.

Contents

List of Figures

List of Tables

Nomenclature

$\vec{A}$	Magnetic vector potential
A_θ	θ-component of the magnetic vector potential
A_θ^*	Nondimensional magnetic vector potential in the θ-direction
A_G	Grid area
$A_{\theta,ref}$	Reference magnetic vector potential
$\vec{B}$	Magnetic flux density vector
$\|\vec{B}\|$	Magnitude of the magnetic flux density
$\|B_r\|$	Magnitude of radial component of the magnetic flux density
$\|B_z\|$	Magnitude of axial component of the magnetic flux density
B_r	Radial component of the magnetic flux density
B_z	Axial component of the magnetic flux density
B^*	Nondimensional magnetic flux density
C_o	Primary electron utilization factor
$\vec{D}$	Electric displacement vector
D	Diameter of the discharge chamber
dl	Element length in respective directions
d_a	Loop anode diameter
d_c	Diameter of cathode
$\vec{E}$	Electric field vector
$\|e\|$	Magnitude of the charge of an electron
$\vec{F}_{mag}$	Lorentz force
g	Acceleration due to gravity
$\vec{H}$	Magnetic field vector
$\vec{H}_c$	Coercive force
H_{cr}	Coercive force component in the radial direction
H_{cz}	Coercive force component in the axial direction
I_{sp}	Specific impulse
$\vec{J}_f$	Free current

k	Boltzmann's constant
l	Path length of primary electron travel during the time step
l_a	Length of the Discharge chamber
l_r	Upstream distance from grids to the magnets
l^*_{ave}	Nondimensional discharge chamber confinement length
L	Lagrangian operator
L_r	Larmor radius
L^*_r	Nondimensional Larmor radius
L_{ref}	Reference length
M_θ	Angular momentum
M^*_θ	Nondimensional angular momentum
$M_{\theta,ref}$	Reference angular momentum
m	Mass of electron
m_n	Mass of neutral particle
$\dot{m}_p$	Propellant mass flow rate
n	Number density of particles
n_{pe}	Primary electron number density
$n_{pe,max}$	Maximum primary electron number density
n^*_{pe}	Nondimensional primary electron number density
n_n	Number density of the neutral particles
N	Total number of particles
P_u	Probability that the primary electron does not have a collision
q_i	Generalized coordinates for Lagrange equations
r	Radial position
$\hat{r}$	Unit vector in the radial direction
r^*	Nondimensional radial position
s	Relative position of primary electron in the axial direction
t	Relative position of primary electron in the radial direction
t_{ref}	Reference time
t^*	Nondimensional time

$t^*_{conf,j}$	Nondimensional confinement time for each primary electron
T	Kinetic Energy
T_e	Electron temperature
T_n	Neutral particle temperature
T_{se}	Secondary electron temperature
u_{eq}	Exit velocity of the propellant
U	Potential energy
$\vec{V}$	Velocity of the primary electron
$\|\vec{V}\|$	Magnitude of the primary electron velocity
V_d	Discharge voltage
V_n	Velocity of the neutral particles
V_r	Velocity component in the radial direction
V_z	Velocity component in the axial direction
V_θ	Velocity component in the azimuthal direction
V^*_r	Nondimensional velocity component in the radial direction
V_{ref}	Reference Velocity
V^*_z	Nondimensional velocity component in the axial direction
V^*_θ	Nondimensional velocity component in the azimuthal direction
z	Axial position
Z_m	Spacing between the magnets
$\hat{z}$	Unit vector in the axial direction
z^*	Nondimensional axial position
$\alpha_1, \alpha_2, \alpha_3, \alpha_4$	Fitted coefficients in the finite element shape function
Δt	Time step increment
Δt^*	Nondimensional time step increment
Δt^*_{lower}	Nondimensional lower limit of time step
Δt^*_{upper}	Nondimensional upper limit of time step
Δt^*_{use}	Nondimensional time step used in Runge-Kutta method
$\Delta t^*_{element,j}$	Residence time spent by primary electron in an element
η	Propellant utilization efficiency

$\hat{\theta}$	Unit vector in the azimuthal direction
λ	Mean free path
λ^*	Nondimensional mean free path
$\vec{\vec{\mu}}$	Permeability of the medium
ρ_f	Free charge density vector
σ_o	Total inelastic collision cross-section
σ_n	Collision cross-section of neutral atoms
ϕ_n	Grid transparency to neutral atoms
ϕ_o	Grid transparency

Acknowledgement

I express my sincere gratitude to all those who directly and indirectly helped me complete this work. Foremost, I thank God, the author and finisher of my faith, for this opportunity and His providence of the required ability without which the completion of this work would have been impossible.

I thank my research advisor, Dr. James A. Menart, whose advise, vision, and guidance facilitated the completion of this work. It was immensely pleasurable working with him. I express my gratitude to Michael J. Patterson and Dr. Thomas J. Stueber from NASA Glenn Research Center, Cleveland, Ohio, for their continued support and guidance.

I thank Dr. Ruby P. Mawasha and Dr. Ravi C. Penmetsa for their willing participation to serve on my thesis committee. I would like to thank my colleagues, Shirin Deshpande and Sudhakar Mahalingam, for freely providing all required knowledge and direction, as well as Tim Leger, who helped me use the workstation cluster.

Most especially, I would like to give special thanks to my love Dr. Gmerice Hammond, my loving brother Kehinde Ogunjobi, my mother Dr. Keji Oyeleke, and my sisters Lola Adeyeye and Olaitan Ogunjobi. Their prayers and encouragements immensely enabled me complete this thesis.

Dedicated to

the men in my life. Taiwo J. Ogunjobi (aka TJ) my late father and a great man I was privileged to call dad, and Kehinde Ogunjobi, my wonderful twin brother and better-half.

1. Introduction

1.1 Electrical Propulsion Thrusters

In 1911, Konstantin Eduardovitch Tsiolkovsky (1857–1935) envisioned and theorized the ion rocket as he discovered the importance of rocket exhaust velocities and the existence of extremely fast particles in the earlier invented cathode ray tubes (Choueiri, 2004). Although the concept of positive charged atomic sized ions had not been established yet, in 1924, Tsiolkovsky suggested using electricity to "produce a powerful flux of ionized helium to serve spacecraft". Writing his thoughts into his notebook in September 1906, Robert Hutchings Goddard (1882–1945) also considered the possibility of electric propulsion when he stated that "reaction with electrons moving with the velocity of light" was plausible. He posed the question: "at enormous potentials can electrons be liberated at the speed of light"? Like Tsiolkovsky, Goddard was aware of the recent developments in the physics of cathode rays, but the insufficient state of that knowledge prevented him from answering his questions. In the subsequent years following these early visionaries, other pioneers practically developed the electric propulsion thruster. Electric propulsion (EP) is a form of rocket propulsion that converts electrical energy into thrust via the generation of a plasma and the electrostatic acceleration of ions. Although EP thrust limitations

previously hindered enthusiasm towards improving this technology, it has presently been revisited and developed because of increased space activity, and the interests in decreasing launch costs and spacecraft longevity. Present EP thrusters include hall thrusters, magnetoplasmadynamic (MPD) thrusters, and electrostatic electron bombardment thrusters such as xenon-ion propulsion systems (XIPS) which is studied in this work.

The advantages and limitations of EP thrusters in comparison to other propulsion systems illustrate their present application. The electrical propulsion thrusters listed above have higher specific impulse relative to other conventional propulsion systems like chemical propulsion thrusters. Specific impulse, I_{sp}, states the effective utilization of propellant by stating the ratio of the thrust produced to the weight of the propellant used. Chemical propulsion thrusters have specific impulses of approximately $250 - 400 seconds$, thus EP thrusters are more propellant efficient as their specific impulse is in the $2,000 - 20,000 seconds$ range. The effective propellant utilization of EP thrusters allows for almost a 90% reduction in the weight of the spacecraft since a relatively small amount of propellant is needed. EP thrusters have higher specific impulses but they generate low thrust since the propellant mass flow exiting the thruster is low, even though propellant exhaust velocities are extremely high. Given their low thrust, EP thrusters are commonly used for satellite station keeping where the low thrust is adequate to correct for solar or lunar gravity tug or reposition a satellite into proper orbit and altitude. Their low thrust also minimizes altitude disturbances during thruster operation. Xenon-ion propulsion thrusters have been used on satellites such as Deep Space 1. Although EP thrusters give low thrust, a sustained thrust time allows it to propel spacecrafts to higher ultimate speeds than a chemical propulsion

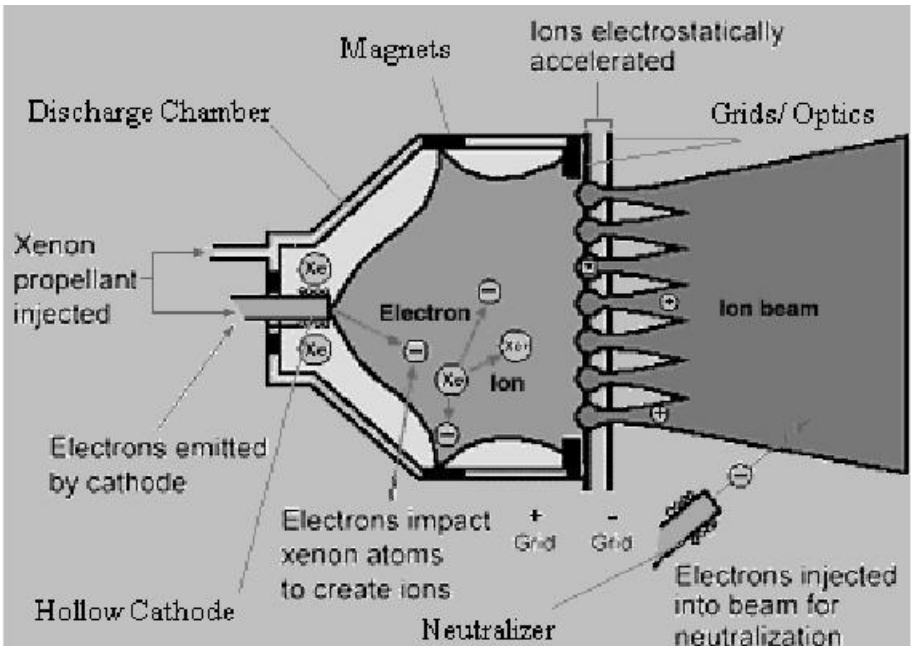

Figure 1.1: Schematic of an ion engine. (Ref. www.nasa.gov)

system.

1.2 Xenon-Ion Propulsion System (XIPS)

A xenon-ion propulsion thruster, as the name suggests, uses the inert gas xenon as the propellant because of its high molecular weight and low ionization potential. In an ion engine, thrust is generated by ionizing neutral gas atoms and then electrically accelerating the ions and ejecting them out the rear of the engine. The working principle of an ion engine entails electron emission, propellant ionization, electrostatic ion acceleration, and ion neutralization. To aid in a brief description of these working principles, a schematic of an ion engine is shown in Fig. 1.1.

Contained within the confined space called the discharge chamber, is a hollow cathode

that discharges electrons when a voltage is applied. The emitted electrons from the cathode, called primary electrons, bombard neutral xenon gas atoms fed into the chamber's space. Ionization of the xenon gas occurs as the emitted high velocity primary electrons bombard xenon atoms to produce, among other particles, positive ions. The ionization collisions generate a plasma within the thin-walled chamber. The generated positive ions within the contained plasma are electrostatically accelerated by the voltage applied across the screen grids at the rear of the discharge chamber. The grids are two parallel perforated plates with a high potential difference. The accelerated ions that are attracted by the charged grids are ejected at very high velocities through the perforations, thereby producing thrust. The last stage in the operation of an ion engine involves neutralizing the ejected positive ions by introducing electrons via a cathode located at the rear of the discharge chamber.

1.3 Scope and Importance of Work

An essential component of an ion engine are the permanent magnets situated on the walls of the discharge chamber as shown in the engine schematic in Fig. 1.1. Utilizing a magnetic field is necessary to prevent unneeded quick electron absorption by the anode biased chamber wall. Since moving charges, such as electrons in the plasma, change direction upon encountering a magnetic field, magnetic fields are thus introduced to divert electrons heading towards the chamber walls. Consequently, if the high energy primary electrons are retained long enough within the discharge chamber, they contribute more to propellant ionization. The increase in ion production improves the derived thrust since more ions are electrostatically accelerated and ejected. In light of this, this work aims to maximize the retention of

primary electrons within the discharge chamber of a xenon-ion propulsion (XIPS) thruster, by optimally configuring the permanent magnets that produce the magnetic field. Thus, the confinement length, the total time an electron spends within the discharge chamber, is the performance parameter used to measure the performance of the discharge chamber ion thruster studied here. It should be noted that although this work surveys magnet circuit configurations on XIPS, the results are applicable to any type of thruster whose chamber confines plasma. Different magnet arrangements have been considered, but it presently appears that the ring-cusp configuration is the dominant magnetic field configuration type utilized on axi-symmetric discharge chambers. The ring-cusp magnet arrangement pattern surveyed in this work is discussed in detail in Chapter 3 Section 3.1 on page 29.

Optimization of the magnet circuit of an ion thruster is performed computationally since it is relatively more cost effective and time efficient than experimental optimizations. Computational modeling of an ion thruster is presented in the next chapter. The confinement ability of different ring-cusp magnetic fields in the discharge chamber of an ion engine is computed by first modeling the magnetic field produced by the permanent magnets, and then modeling the trajectories of the primary electrons as they interact with the magnet field.

2. Computational Modeling Tools

Computationally modeling the discharge chamber involves modeling the magnetic field of a two-dimensional cross-section of the a discharge chamber-magnet configuration, followed by modeling the primary electron trajectories within the chamber. The magnetic field modeling code, MAXWELL 2D, and the primary electron trajectory modeling code, PRIMA, are the computational modeling tools utilized for the confinement optimization surveys in this work. In this chapter, an overview of both computational tools are presented in Section 2.1 and 2.2 respectively. Then a discussion on the history of the trajectory path modeling (Section 2.2.2), is followed by a brief description of the mathematics contained in both modeling tools (Section 2.1.2 and 2.2.4). The solution methods and techniques utilized in solving the primary electron mathematical model are briefly explained (Section 2.2.4), and the output data for the primary electron trajectory modeling code, PRIMA, is then discussed (Section 2.2.5). To validate the accuracy of PRIMA, a brief comparison between computational and experimental results is discussed in Section 2.2.3. Data interfacing between both computational tools is briefly described in Section 2.1.1.

2.1 Magnetic Field Modeling Tool

2.1.1 MAXWELL 2D - A Magnetic Field Solver

Maxwell 2D, developed by the Ansoft Corporation (MAXWELL 2D, 2004), is an electromagnetic simulation software program that can be used to simulate a two-dimensional magnetic field. The surveys in this work use this software to obtain the two-dimensional magnetic vector potential produced by an input chamber-magnet layout. It should be noted that in the radial and axial plane space used, the magnetic vector potential in the circumferential direction is constant. Maxwell 2D is a finite element solver that discretizes a selected domain into triangular elements, assigns provided boundary conditions, and computes the required output quantity at each element node. To improve accuracy, MAXWELL 2D has also an adaptive grid solver such that the field simulator automatically increases the density of the previously generated mesh and recomputes the field quantities until the solution is sufficiently mesh independent. To obtain sufficient accuracy in all surveys, the finite element mesh was automatically refined until the magnetic vector potential field registered a 0.6% percentage error between sequential computational passes. Thus, MAXWELL 2D automatically provides a converged magnetic vector potential field. The primary feature used to determine the accuracy of the field solution is the solvers residual plot generated by MAXWELL 2D. The residual plot shows how well the field solution satisfies the appropriate form of Maxwell's equation. Nodal value computations are reiterated for residuals less than a selected target value. Essentially, MAXWELL 2D provides an exact solution of the magnetic field produced by axi-symmetric, permanent magnets.

In using Maxwell 2D, a radial and axial plane space is selected as the drawing type, and since the magnetic field is produced by permanent magnets, a magnetostatic solver is selected. The geometry of the discharge chamber-magnet configuration is drawn into the two-dimensional radial and axial plane space. The geometry of a chamber-magnet configuration must consist of straight lines since the primary electron modeling code, PRIMA, utilizes these type of geometries. Next, material properties are assigned to the objects contained in the geometric model. The material properties and specifications used for surveys in this work are presented in Chapter 3 in Section 3.2. A more detailed summary for using MAXWELL 2D is presented by Deshpande and Menart (2004).

2.1.2 Magnetic Field Mathematical Model

The magnetic field modeling tool, MAXWELL 2D, models the static magnetic field by solving Maxwell's equations. The general form of Maxwell equations relate the spatial derivatives of the magnetic and electrical magnetic fields to their time derivatives and external and internal sources as shown in Eqns. (2.1) to (2.4).

$$\vec{\nabla} \cdot \vec{D} = \rho_f, \tag{2.1}$$

$$\vec{\nabla} \times \vec{E} = -\frac{\partial \vec{B}}{\partial t}, \tag{2.2}$$

$$\vec{\nabla} \cdot \vec{B} = 0, \tag{2.3}$$

and

$$\vec{\nabla} \times \vec{H} = \vec{J_f} + \frac{\partial \vec{D}}{\partial t}, \tag{2.4}$$

The magnetic field provided by the free current from the potential applied to the plasma is neglected in this model since it is insignificant relative to the field provided by the permanent magnet sources. To further simplify the analysis, since only the steady state operation of the chamber is considered, the time change of the magnetic induction $\frac{\partial \vec{B}}{\partial t}$ and the electric displacement $\frac{\partial \vec{D}}{\partial t}$ are set as zero. Applying the above stated assumptions that the free current $\vec{J}_f$ is zero, and the chamber operation is steady, Maxwell's equations for a two-dimensional axi-symmetrical cylindrical coordinate system is reduced to Eqn. (2.5).

$$\left(\frac{\partial H_{cr}}{\partial z} - \frac{\partial H_{cz}}{\partial r}\right) = \frac{\partial}{\partial r}\left(\frac{1}{r\mu}\frac{\partial (rA_\theta)}{\partial r}\right) + \frac{\partial}{\partial z}\left(\frac{1}{\mu}\frac{\partial (A_\theta)}{\partial z}\right). \tag{2.5}$$

A more detailed reduction of Maxwell equations from its general form is presented by Deshpande and Menart (2004). The required boundary conditions for use with Eqn. (2.5) are

$$\begin{aligned} &A_\theta \to 0 \quad as \quad r \to \infty && A_\theta \to 0 \quad as \quad z \to -\infty \\ &\frac{\partial A_\theta}{\partial r} = 0 \quad at \quad r = 0 && A_\theta \to 0 \quad as \quad z \to \infty. \end{aligned} \tag{2.6}$$

The magnetic vector potential, determined from the solution of Eqn. (2.5), is exported on a grid, to a short program written by Mahalingam that converts it to the magnetic flux density input data required for the primary electron trajectory modeling tool. Details of this interfacing is presented by Deshpande (1995). The magnetic flux densities in the radial and axial direction, B_r and B_z, are obtained by taking the appropriate derivatives of the magnetic vector potentials,

$$B_r = \frac{1}{r}\frac{\partial (rA_\theta)}{\partial r} \qquad and \qquad B_z = \frac{\partial A_\theta}{\partial z}. \tag{2.7}$$

2.2 Primary Electron Tracking Modeling Tool

2.2.1 PRIMA - A Particle-in-Cell Code

PRIMA, initially developed by Arakawa and Ishihara (1991), is a FORTRAN 77 code that tracks primary electrons within the plasma generated in an axi-symmetric discharge chamber with straight walls. The trajectories of numerous electrons are tracked using a particle-in-cell simulation technique. The primary assumptions in PRIMA are that only primary electrons are tracked, primary electron collisions are elastic, and plasma electric fields are ignored. The corresponding justification for each assumption follows.

In addition to primary electrons emitted from the cathode, other constituents of a plasma are secondary electrons, electrons displaced from neutral atoms, and ions, positive particles missing an electron. Although, like primary electrons, secondary electrons contribute to ionization, for computational simplicity only primary electrons are tracked by PRIMA. Primary electrons possess higher energies relative to secondary electrons and thus ionize neutral xenon atoms much more readily than secondary electrons. In addition, primary electrons start the ionization process. They are the most important electrons to keep inside the chamber. In order to keep the discharge burning, some secondary electrons must be absorbed by the walls. For these reasons only primary electrons are tracked with PRIMA. The veracity of this assertion is evident in the preceding Section 2.2.3 where the computational results of PRIMA are compared with experimental results.

In modeling the primary electron trajectory with PRIMA, ionization collisions are not considered and only a change in direction of the primary electron occurs in their collisions

with neutral atoms, with singly charged positive ions, with the chamber walls, or with the grids. In these elastic collisions, kinetic energy is conserved as there is no absorption or energy transfer between colliding particles. Since particle collisions such as ionization collisions are inelastic where momentum but not kinetic energy is conserved, modeling particle collisions as elastic precludes atom ionization in the plasma. Although PRIMA can handle inelastic ionization collisions, these collisions are not included in the analysis. The inclusion of ionization collisions in PRIMA would shorten the computed confinement length, thus skewing the actual length of time a primary electron is confined within the chamber to shorter values. Brophy and Wilbur (1985) have stated that inelastic collision should not be included in the determination of the confinement length. Including ionization collisions produces an unfair comparison between different magnetic field configurations. In addition, the assumption of elastic collisions in PRIMA maintains computational simplicity. The assumption of elastic collision is also necessary because they are responsible for driving electrons across the magnetic field lines. If no collisions are considered confinement lengths would approach infinity.

In PRIMA, the electric fields that occur in the thin plasma sheath generated just inside the discharge chamber walls are ignored. In the plasma sheath, the potential difference between the plasma and anode-wall voltage is shielded from the plasma's interior. PRIMA neglects the electrical fields since computational complexities are introduced as all particles and their complex interactions that affect the electrical field would have to be modeled. In addition, Mahalingam's (2005) ongoing research work is showing that electric fields influence confinement lengths.

In modeling the primary electron trajectory, specular reflections occur for primary electron collisions with the centerline and the grids. Based on the objective of a given chamber-magnet configuration survey, the chamber walls can be specified as reflective or absorbing. Cathode biased walls are specified as reflective, electron wall collisions are considered elastic, with the electron reflected at an angle equal to the incidence angle. For chamber walls specified as anode biased, primary electron are absorbed, and this destroys the electron and terminates its confinement length. A manual on using the version of PRIMA utilized in this work has been written by Ogunjobi (2005).

2.2.2 Literature Survey and History of PRIMA

Over the years, computational modeling tools have been developed to model the ion engine discharge chamber. Presented in this section is the history of this development and progression.

The first computational modeling tool for analyzing the performance of an ion engine was developed by Brophy and Wilbur (1985). In their model developed for high flux density ring cusp magnetic field ion thrusters, the engine performance was computed in terms of configuration and propellant dependent parameters, as well as operating parameters. In the computation, the primary configuration and propellant dependent performance parameters used are the electron confinement length, the baseline plasma ion energy cost, the extracted-ion fraction, and the cathode potential surface ion fraction. The operating parameters used are the parameters used were the propellant mass flow rate and the cathode discharge voltage. The computational model showed that engine performance depended

on the primary electron confinement length and the baseline plasma ion energy cost when the same propellant and grid transparencies are used. Unlike the computational modeling tool used in this work, in Brophy and Wilbur's model the confinement length was an input parameter obtained from other computational models. To obtain ion engine performance, Brophy and Aston (1989) used this computational model of Brophy and Wilbur (1985). Again, Brophy and Wilbur's model was used by Wilbur et al. (1990) to calculate the performance of an ion engine when input parameters describing the performance of certain components of the engine are entered. The grid system, the primary difference from Brophy and Wilbur's model, included the physical constraints from the span-to-span ratio, the discharge power per unit beam area, and the grid electric field.

A computational model of the plasma in the discharge chamber was developed by Arakawa and Wilbur (1988). Their computational tool first involved obtaining the magnetic field via a finite element method, and then modeling a two-dimensional plasma that described the generation and diffusion of electrons and ions in the chamber. Arakawa and Wilbur modeled the plasma by solving the diffusion equations with a spatial variation of the diffusion coefficient. The primary electron number density needed for the solution of the equations describing the plasma, was estimated by ignoring collisions and the trajectory of the electrons. In addition, a constant electron temperature and neutral atom density was assumed throughout the discharge chamber. The primary outputs used to illustrate engine performance with respect to a given magnetic field configuration, were the ion flow fractions to the wall surface of the chamber, the extracted-ion fractions, and the plasma density distribution.

One of the first detailed computational models of the primary electrons in the plasma contained in a discharge chamber was developed by Arakawa and Yamada (1990). Their model, PRIMA, used a Monte Carlo technique to track the primary electrons within a right-cylindrical chamber with a ring-cusp magnetic field. The average confinement length of the primary electron was a determinable output. The validity of Arakawa and Yamada's computational tool was determined by a comparison between results obtained and experimental results. A good comparison was obtained when particle and anomalous collisions were modeled, and an unsatisfactory comparison resulted when only particle collisions were modeled. There are some questions about the validity of this comparison, however, because of the parameters that Arakawa and Yamada could tweak in their analysis.

Arakawa and Ishihara (1991) developed a theoretically detailed computational model of the plasma contained in a right-cylindrical discharge chamber of cusped ion thrusters. In addition to calculating and outputting the relative primary electron number density, the ion number density, and the ion production cost, their model, unlike previous models, calculated the primary electron confinement length as well. The other outputs provided where the beam ion production cost, the primary electron utilization factor, and the neutral absorption rate. These outputs were based on assumptions of the grid performance. This model provided plasma performance values with no input performance assumptions. In Arakawa and Ishihara's computational modeling of the plasma, the plasma density distribution was obtained from Arakawa and Wilbur's (1988) computational model, the electron trajectories were obtained using Arakawa and Yamada's (1990) model, and the discharge chamber performance analysis was obtained from Brophy's (1985) model.

To simulate charged particle motions in the cusp region of a magnetic field in an ion thruster, Hirakawa and Arakawa (1993) modified Arakawa and Ishihara's (1991) computational code to include the electric field present in the plasma. Although plasmas are mostly electrical neutral, there exists electric fields near the chamber walls. In computational modeling of the interactions of charged particles with the approximated magnetic field and the electrical field with their two-dimensional particle-in-cell (PIC) code, particle collisions were ignored and the ions were generated outside the cusp region by ionizing collisions between neutral atoms and primary electrons. Similar outputs to those obtained from Arakawa and Ishihara's (1991) model are obtained here.

Arakawa and Yamada's (1991) computational modeling tool PRIMA, keep track of the primary electrons interacting with a magnetic field in an axi-symmetric chamber. PRIMA has subsequently been modified by Mahalingam and Menart (2003). The modifications enables PRIMA to handle any discharge chamber composed of straight-line walls. To expand PRIMA's range of applicability, Mahalingam and Menart corrected some inaccuracies carried on from Arakawa and Ishihara's (1991) initial development of this code. In addition, the modifications included implementing parallel computing capabilities to improve the computational speed since the renormalization of the velocities, as done by Arakawa and Yamada (1990) and Arakawa and Ishihara (1991) were eliminated. The improvement of the computational speed by parallelization, also allowed the use of smaller time steps which improved modeling accuracy. Mahalingam and Menart's modified version of PRIMA is the plasma modeling computational tool used in the surveys in this work. The previous and subsequent sections present a detailed explanation of Mahalingam and Menart's PRIMA.

Wirz and Katz (2005) developed a two dimensional computational model of the plasma contained in a discharge chamber with a ring cusp magnetic field configuration. This model is perhaps the most developed computer model of the discharge chamber. In comparison to other models, non-uniform plasma, neutral atom distributions, and straight-line neutral atoms trajectories were considered. A finite element method was used to obtain the magnetic field where the elements were made to run along the magnetic field lines.

2.2.3 Accuracy of PRIMA

To establish confidence in the computational results obtained from PRIMA, a comparison between PRIMA results and experimental results from a cusp anode discharge chamber (Hiatt and Wilbur 1986) was performed by Deshpande and Menart (2004). In discussing the veracity of PRIMA, the results of the comparison are first stated; and then the experimental and computational geometries and the relatively insignificant differences between them follow.

Given that not all physical phenomenon that occur within the plasma are modeled, and also the assumption of inelastic collisions for the primary electrons, PRIMA nevertheless possess reasonable accuracy. The largest deviation of the computational values from the experimental results is small. Deshpande and Menart (2004) showed that for varying neutral number density parameters, the percentage difference between computationally and experimentally obtained plasma ion energy costs, ϵ_p, was no greater than 18%. This relatively small difference can be seen in Fig. 2.1 which plots the plasma ion energy cost against the neutral number density parameter for PRIMA's computational results, Hiatt and Wilbur's

experimental results, and Brophy's theoretical results. An indicator of the density of the neutral atoms in the plasma, the neutral number density parameter, is given as $\dot{m}_p(1-\eta)$ where $\dot{m}_p$ is the propellant mass flow rate, and η is the propellant utilization efficiency. Brophy's curve is a theoretical curve that uses a constant primary electron utilization factor, C_o. Since the utilization factor varies with neutral number density parameter in reality, there is a slight deviation of the experimental and computational values from the theoretical values for higher neutral number density parameters. The primary electron utilization factor, C_o,

$$C_\circ = \frac{4\,\sigma_\circ\,\lambda_{ave}}{|e|\,V_n\,\phi_n\,A_g} \tag{2.8}$$

gives the degree to which primary electrons interact with neutral atoms. In this equation σ_o is the total inelastic collision cross section, λ_{ave} is the average confinement length, V_n is the velocity of the neutral particles, ϕ_n is the grid transparency to neutral particles, and A_g is the area of the grid.

The performance parameter compared, the plasma ion energy cost, is the average amount of energy required to produce an ion. Although the confinement length is the primary performance parameter considered in surveys in this thesis, the use of the plasma ion energy cost for comparison was legitimate since it is indirectly proportional to the confinement length. As seen from Eqn. (2.9),

$$\epsilon_p = \epsilon_p^*[1 - e^{-C_o\dot{m}_p(1-\eta)}]^{-1}, \tag{2.9}$$

the plasma ion energy cost ϵ_p is proportional to the primary electron utilization factor, C_o, which in turn is proportional to the average confinement length of the electrons, λ_{ave} (Eqn. (2.8)). Since PRIMA only calculates the utilization factor, C_o, the corresponding

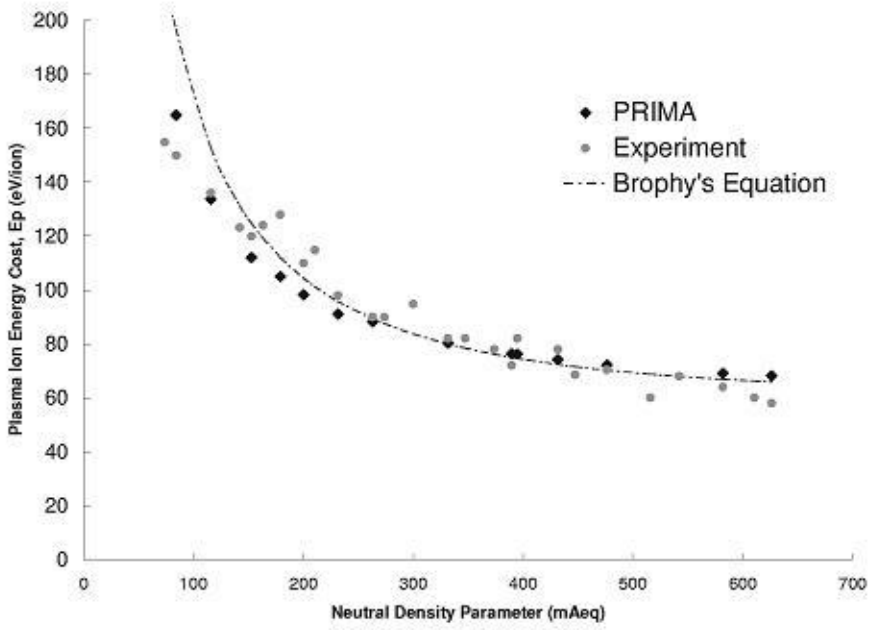

Figure 2.1: Plot of experimentally and computationally obtained ion energy cost versus neutral number density parameter (Deshpande 2004).

plasma ion energy cost was calculated using Eqn. (2.9). To obtain the baseline plasma ion energy cost ϵ_p^*, the entire plasma would have had to be modeled. Since PRIMA does not model all phenomenon within the plasma, the baseline plasma ion energy cost of $62eV/ion$ was obtained from Hiatt and Wilbur's experimental results. Furthermore, for the computational calculation of the plasma ion energy cost, the propellant mass flow rate $\dot{m}_p$ and utilization efficiency η were exactly those used in the experiment.

Discharge Chamber Geometry	
Discharge chamber inner diameter	9.2 cm
Length of the discharge chamber (l_a)	11.8 cm
Thickness of the discharge chamber walls	0.64 cm
Upstream distance from the grids to side magnetic rings (l_r)	3.7 cm
Rare earth magnet dimension	1.3 cm $\times 0.5cm$
Operating Specifications	
Discharge voltage (V_d)	50 Volts
Propellant	Argon
Propellant mass flow rate ($\dot{m}_p$)	100 - 700 mA
Beam diameter	8 cm
Grid transparency to neutral atoms	0.54
Grid transparency to ions	0.68
Distance between screen grid and cathode	1.5 cm
Flux Density on surface of magnetic rings	0.27 Tesla
Discharge chamber wall material	Steel
Baseline plasma ion production cost (ϵ_p^*)	62 eV/ion

Table 2.1: Geometric and operating specifications for Hiatt and Wilbur's (1986) experimental ion engine.

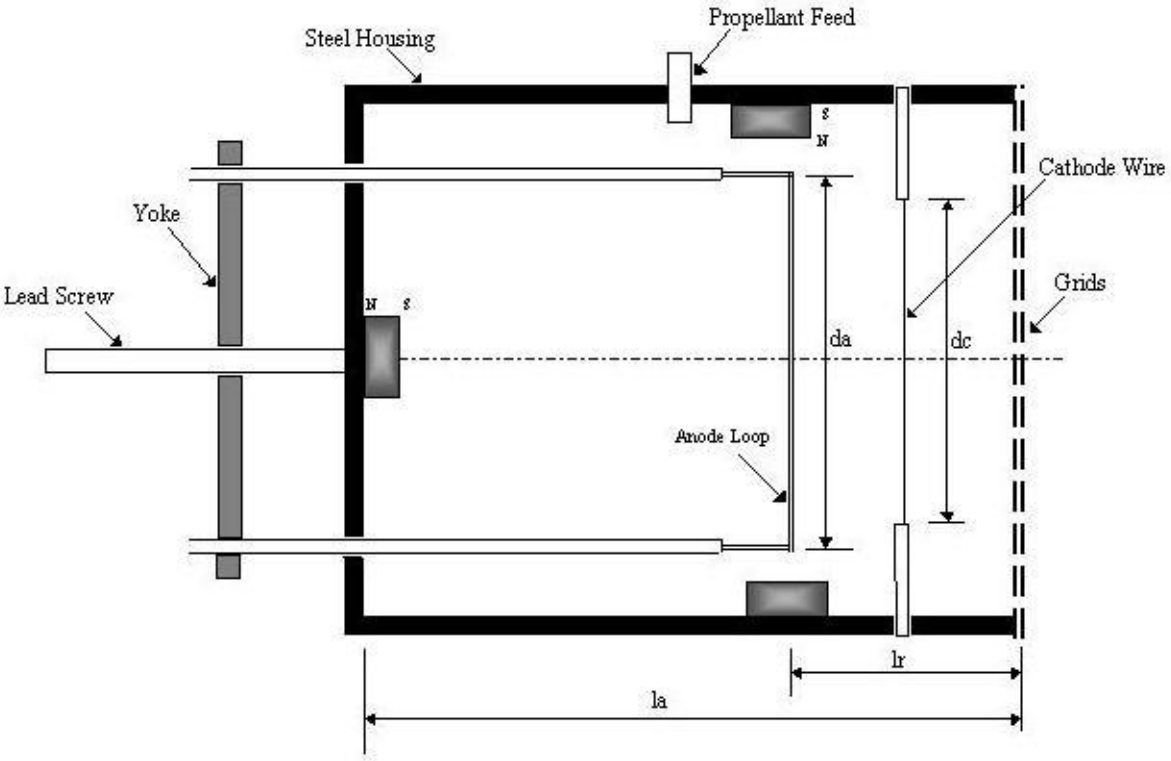

Figure 2.2: Hiatt and Wilbur's (1986) experimental ion engine.

The cusp anode model studied by Hiatt and Wilbur (1986) is shown in Fig. 2.2 and the geometric and operating specifications used are listed in Table 2.1. Except for a few differences, the computational model Deshpande used in PRIMA's cusp anode model utilized identical values. One difference between the experimental and computational setup, was the possible difference in the chamber housings used. Although Haitt and Wilbur's model does not specify the steel type used for the housing, the 1010 steel Deshpande uses does not adversely alter the magnetic field from that used by Haitt and Wilbur. In Hiatt's cusp anode study, the anode was a $0.25mm$ thin steel sheet attached to the side magnet ring surfaces (cusp region) with a $0.76mm$ flexible mica sheet. The mica sheet is not mod-

eled in PRIMA. Also in Hiatt's model, the axially variable anode loop was removed and the thermionic cathode was a thin, toroidal wire held by a support structure. Although a support structure was not modeled in PRIMA, the effects of this difference is negligible since the support structure occupies a minute fraction of the discharge chamber. The last negligible difference between both models is that in PRIMA, the primary electrons from the cathode are emitted into a uniform neutral particle distribution within the chamber. In the physical model, the propellant feed is localized (see Fig. 2.2) and the neutral atom distribution is thus not uniform throughout the chamber.

2.2.4 Primary Electron Tracking Mathematical Model

In PRIMA, the primary electron motion is computed from the non-dimensional equations of motion. A detailed derivation of the equation of motion and the required initial conditions are discussed here but presented in more detail by Deshpande and Menart (2004). Other important mathematical equations presented are the equations from which the number densities of the plasma particles are obtained and the probability function by which PRIMA determines particle collisions.

The basic equation of motion that models the trajectory of the primary electrons within a magnetic field is derived from Lagrangian mechanics. The sum of the Lagrangian over time defines the trajectory of the primary electron. It should be noted that in the Lagrangian derivation of the equation of motion for the charged particles in a magnetic field, the motion of the particle due to the magnetic field is considered as potential energy (Greenwood, 1997). The radial, axial, and circumferential equations of motion for axi-symmetric coor-

dinates are

$$m\frac{dV_r}{dt} = m\frac{V_\theta^2}{r} - |e|\frac{V_\theta}{r}\frac{\partial\,(r\,A_\theta)}{\partial r} \tag{2.10}$$

$$m\frac{dV_z}{dt} = -|e|\frac{V_\theta}{r}\frac{\partial\,(r\,A_\theta)}{\partial z} \tag{2.11}$$

$$M_\theta = m\,r\,V_\theta - |e|\,r\,A_\theta. \tag{2.12}$$

Although the coordinate is axi-symmetric, the circumferential direction of the primary electron has to be included in the equations of motion.

Equations (2.10) and (2.11) are statements of Newton's Law in the radial and axial directions, and Eqn. (2.12) states that angular momentum is conserved. The first term on the right-hand side of the radial equation of motion is the centrifugal acceleration that occurs in a cylindrical coordinate system, and the first term on the right hand side of the circumferential equation (Eqn. 2.12) is the angular momentum of the primary electron. The inertia terms in the radial and axial directions, are included on the left hand sides of Eqn. (2.10) and Eqn. (2.11) respectively. The term on the left-hand side of Eqn. (2.12) is a constant that only changes when the primary electron undergoes a collision with another particle or with a wall. In addition to the primary electron's basic motions and collision, the only other included effect on the motion of the primary electron is the magnetic field. A charged particle moving in a magnetic field is accelerated in a direction that is perpendicular to the direction of its own velocity and the direction of the magnetic field. This interaction between the moving primary electron and the magnetic field exerts a Lorentz force on the primary electron. With the Lorentz force acting perpendicular to the direction of the velocity of the electron, the direction of motion of the particle is thus changed upon encounter with a magnetic field. This magnetic field contribution to the motion of the primary electrons is

included in the second term on the right hand side of Eqn. (2.10) and Eqn. (2.12), and in the only term on the right-hand side of Eqn. (2.11).

The initial conditions for the equation of motions are the initial position and velocity of the primary electron. The magnitude of the initial velocity is determined from the applied discharge voltage V_d as

$$\vec{V} = \sqrt{\frac{2|e|V_d}{m}}, \tag{2.13}$$

and the emission direction, is determined by a Monte Carlo technique discussed in Section (2.2.4), and is such that the electron has a random but uniform distribution in a 2π steradians angle range from the cathode tip. The initial position, which is the specified emission location, is the tip of the cathode.

As stated in Section (2.2.1), collisions of primary electrons with neutral atoms or ions are assumed to be elastic. The number density of the neutral atoms and ions are needed to determine the elastic collisions of primary electrons with these particles. These number densities, n_n and n_i

$$n_n = \frac{4\dot{m}_p(1-\eta)}{|e|V_n\phi_n A_g} \tag{2.14}$$

$$n_i = \frac{\dot{m}_p\eta}{|e|V_i\phi_i A_g}, \tag{2.15}$$

are determined from the propellant flow rate $\dot{m}_p$, the utilization efficiency, η, the velocity of the neutral atoms or ions, V_n and V_i, the transparency of the grids to neutral atoms or ions, ϕ_n and ϕ_i, and the area of the grids A_g.

To determine if there is a particle collision, PRIMA uses a probability function

$$P_u = e^{-\frac{l}{\lambda_u}} \quad \text{where} \quad \lambda_u = \frac{1}{n_n\sigma_n}, \tag{2.16}$$

where λ_u is the mean free path length and l is the distance the primary electron travels during the time step determined from a Runge-Kutta technique (see Section 2.2.4). n_n is the neutral number density (Eqns. (2.14)), and σ_n is the collision cross section of the neutral atom to primary electrons. Deshpande and Menart (2004) and Mahalingam and Menart (2002) both present more detail on the probability equations.

Primary Electron Tracking Mathematical Model Solution Method

The non-dimensional form of the equations of motion utilized by PRIMA is

$$\frac{dV_r^*}{dt^*} = \frac{V_\theta^{*2}}{r^*} - \frac{V_\theta^*}{r^*}\frac{\partial(r^* A_\theta^*)}{\partial r^*} \tag{2.17}$$

$$\frac{dV_z^*}{dt^*} = -V_\theta^* \frac{\partial A_\theta^*}{\partial z^*} \tag{2.18}$$

$$M_\theta^* = r^* V_\theta^* - r^* A_\theta^*. \tag{2.19}$$

All variables in the equation of motion are nondimensionalized by dividing them by the maximum reference values for that variable. The variables and the reference quantities used to nondimensionalize the equations of motion (Eqns. 2.10 to 2.12) are presented by Mahalingam and Menart (2002), and also by Deshpande and Menart (2004).

PRIMA simultaneously solves these nondimensional equations, using different methods and techniques to solve for the different terms. A finite element method is used to determine the spatial derivatives $\frac{\partial}{\partial r}$ and $\frac{\partial}{\partial z}$ of Eqns. (2.17) and (2.18). In this finite element approach, the spatial domain of the discharge chamber is descritized into rectangular bilinear elements, and by using appropriate shape functions and the particle's axial and radial position, the magnetic vector potential A_θ^* is interpolated. The nodal values of the

magnetic vector potential A_θ^* are obtained from MAXWELL 2D. A fourth order Runge-Kutta numerical method is used to solve the first order temporal derivatives, $\frac{dV_r^*}{dt^*}$ and $\frac{dV_z^*}{dt^*}$, in Eqns. (2.17) and (2.18). The initial values required for this propagation are obtained from a Monte Carlo technique. The required nondimensional velocity component in the azimuthal direction, V_θ^* is obtained from Eqn. (2.19). Given the potential instability for the Runge-Kutta propagation scheme, very small nondimensional time step are used. As well as being used to determine the initial values for the finite element technique by determining the direction of primary electron emission from the cathode, the Monte Carlo technique is used to predict if primary electron and particle collisions occur, and the subsequent direction of travel of the primary electron preceding a collision. The probability equation that predicts a collision is presented in Eqn. (2.16). It should be noted that this statistical approach provides invariant results when a large number of primary electrons are tracked. A random number generator generates a random number between 0 and 1; and this number is compared to the value from the probability equation. For values of the random number less than values of the probability function, collisions do not occur. For the reverse, collisions are predicted to occur. Only a brief summary of the solution methods used in PRIMA have been discussed here. More details on the finite element, Runge-Kutta, and Monte Carlo techniques used are discussed by Mahalingam and Menart (2002) and by Deshpande and Menart (2004).

2.2.5 Output Quantities for PRIMA

Of all the results that PRIMA outputs, only the utilized critical outputs are discussed here. The confinement length and the primary electron relative number density are the two major quantities utilized. The operational inputs required for PRIMA are discussed in the next chapter (Section 3.2).

The confinement length is the time span a primary electron remains in the discharge chamber before it is absorbed by an anode biased wall. Given that the velocity in the equation of motion (Eqns. 2.10 to 2.12) is nondimesionalized in PRIMA (Eqns. 2.17 to 2.19), the primary electron nondimensional velocity remains at 1.0. Thus for an individual primary electron, the nondimensional confinement length is equal to the nondimensional confinement time. The average nondimensional confinement length

$$l^*_{avg} = \frac{1}{N}\sum_{j=1}^{N} t^*_{conf,j}, \tag{2.20}$$

is the average of the nondimensional confinement time, $t^*_{conf,j}$, for N primary electrons. To obtain the dimensional confinement length, the nondimensional confinement length is multiplied by the diameter of the discharge chamber.

Another PRIMA output quantity is the nondimensional relative number density, n^*_{pe}, of the primary electrons. This quantity

$$n^*_{pe} = \frac{n_{pe}}{n_{pe,max}} = \frac{\sum_{j=1}^{N} \Delta t^*_{element,j}}{\left[\sum_{j=1}^{N} \Delta t^*_{element,j}\right]_{max}}, \tag{2.21}$$

indicates how the electrons are distributed in the discharge chamber. It is a value that gives the function of the total primary electrons relative to the maximum value at a given spatial

location within the chamber. The fraction is stated as the ratio of the primary electron density at a certain location, n_{pe}, to the maximum number density inside the discharge chamber, $n_{pe,max}$. The ratio is actually calculated using the dimensionless residence times where $\Delta t^*_{element,j}$ is the total time spent by a primary electron in a given element at a given location inside the discharge chamber.

3. Magnet Circuit Configurations

The confinement of primary electrons is greatly improved by introducing magnetic fields which serve to keep the electrons away from the anode biased chamber walls, thereby enhancing their chances of producing an ion. The magnetic fields generated are dependent on the position, location, and orientation of the magnet rings that comprise the magnet circuit. This chapter presents the different ring-cusp magnet circuit configurations surveyed, with the survey results and deduced guidelines presented in the next chapter. An introduction to ring-cusp magnet configurations presented in Section 3.1, begins with a brief look at other magnet circuit arrangements being used on discharge chambers, and it concludes with a detailed description of the ring-cusp magnet configuration type studied here. Many ring-cusp magnet configuration pairs are constructed by varying the magnet location axially or radially, and these configurations are classified by which of either the axial spacing (Section 3.1.1) or radial spacing (Section 3.1.2) of the interacting magnets is varied. Next, the discharge chamber geometric dimensions, its material properties, and the operating specifications for the discharge chamber used in all surveys in this work are presented (Section 3.2). Lastly, based on data from a cusp region study by Deshpande and Menart (2004), and data from the magnet circuit arrangements surveyed, the mechanisms that affect discharge chamber primary electron confinement length, and subsequently engine performance, are discussed (Section 3.3).

3.1 Introduction to Ring-Cusp Magnet Configurations

To improve the discharge chambers electron confinement ability, there have been different magnetic field types constructed by altering the magnet circuit configuration. Some of the earliest magnet circuits used electromagnets (Kauffman, 1984). For example, Brophy and Wilbur (1983), in their experiments, used electromagnets to produce different magnetic fields with varying strengths by simply altering the current flow and wiring of the magnet circuit. Also, the UK-10 ion thruster utilizes electromagnets (DeBoer, 1999). Given the drawback that an electrical power source is needed for electromagnet circuits, most magnet circuits currently use permanent magnets which do not require large power sources. Permanent magnets have a lengthy lifespan and produce good static fields. Some investigated magnetic field types that have used permanent magnets are the divergent magnetic field (Sovey, 1976 and Lovell, 1979), the line-cusp magnetic field (Sovey, 1981), and the ring-cusp magnetic field (Sovey, 1984). As seen in works by Sovey (1984) and Ramsey (1979), it appears that the ring-cusp magnetic field is the dominant type used on axi-symmetric discharge chambers at this time.

The ring-cusp magnetic fields studied here (shown in Fig. 3.1), consist of magnet rings constructed by placing small permanent magnets around the circumference of the axi-symmetric chamber. These rings of magnets can be placed on the front, back, or sidewall of the discharge chamber. The ring-cusp magnet circuit configuration, as the name implies, produces ring-cusps that circle the circumference of the chamber.

For each magnet circuit configuration surveyed, the objective is to develop guidelines that describe the magnet ring spacing, position, and orientation that provide the best con-

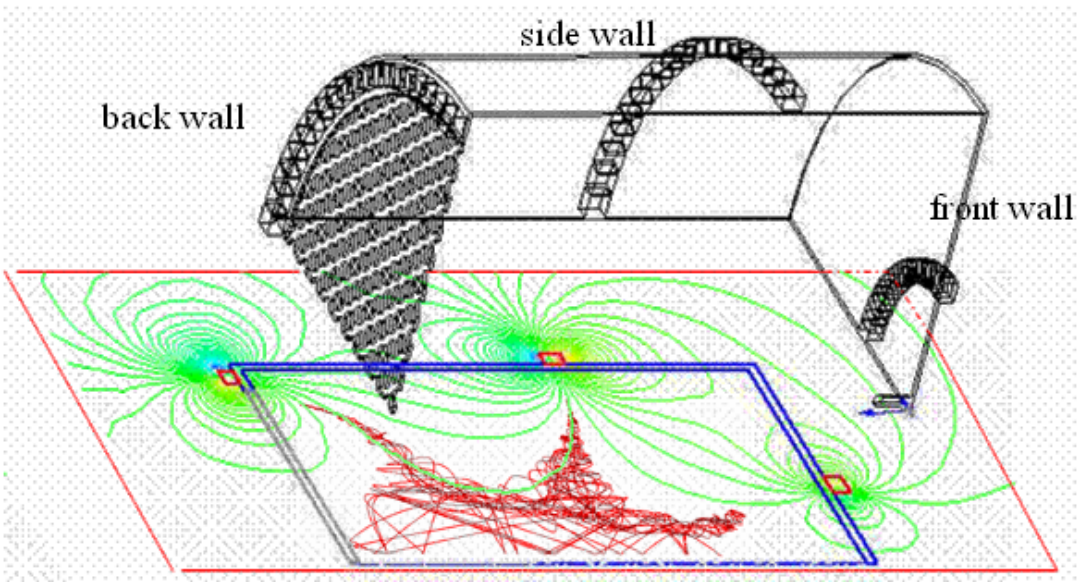

Figure 3.1: Axisymmetric cylindrical discharge chamber with magnet rings forming a ring-cusp magnetic field.

tainment of primary electrons. To keep the guidelines as general as possible, magnet pair configurations are studied. The guidelines obtained for these magnet pair surveys can be combined and applied to obtain complex ring-cusp magnet circuits. The ring-cusp magnet pair configurations surveyed are grouped into an axial or radial class where the axial spacing or radial spacing is the parameter varied. In the axial class, the radial spacing between the magnet pair is fixed based on guidelines obtained from preceding surveys. Similarly, the axial spacing is fixed in the radial class. Two labeling conventions are used to sufficiently describe a magnet pair arrangement. The first convention describes the configuration in terms of the wall on which the magnet is placed. For example, a magnet pair located on the side wall of the discharge chamber is refereed to as a 'side-side' wall pair (see Fig. 3.2). The second convention describes the configuration in terms of the angle between the pole

axis of adjacent magnet rings. For example, since the polarity of adjacent magnets are alternated for the 'side-side' wall pair, there is a 180° angle between the poles. No axial or radial spacing survey is done for a side-back magnet pair because the grids limit the radial position of the back magnet to essentially one radial location.

One of the magnet circuit configuration surveyed includes a magnet ring on a slanted front wall that aims to model the conical-cylindrical chamber used by NASA in its NSTAR program (Polk et al., 1996) and Deep Space One (NASA, 2002).

3.1.1 Magnet Ring Pair with Varying Axial Spacings

Surveys in this class vary the axial spacing between magnet pairs by fixing one or both magnet rings and varying the length of the discharge chamber. Tabulated in Table 3.1 are the configurations surveyed in this class.

A fixed length chamber with varying number of side magnet rings, surveyed by Deshpande et al. (2005), was the first configuration of this class surveyed. In this sole non-pair arrangement, shown in Fig. 3.2, the length of the discharge chamber was fixed at $20cm$, and the axial spacing between the 180° oriented magnets was varied by increasing the number of side magnets. The outermost side magnet rings are positioned $1cm$ from the front and rear walls of the chamber. The objective of this arrangement was to show the effect of the number of magnets and their axial spacings on primary electron confinement length.

Based on the guideline established in the fixed length chamber survey, Deshpande et al (2004) concluded that a refined survey for side magnet axial spacing was necessary. A

Class	Pair Location	Variable	Orientation	Figure	Results
Axial	Side Wall	Number of Side Wall Magnet Rings	180° †	3.2	Section 4.1.1
	Side-Side	Axial Spacing	180° †	3.3	Section 4.1.2
	Front-Side	Front Wall Magnet Orientation and Axial Spacing	90° ‡, 120°, 150°	3.4	Section 4.1.3
	Front-Back	Axial Spacing	0°	3.5	Section 4.1.4
	Side-Back	Axial Spacing	90°	3.6	Section 4.1.5
Radial	Front-Side	Front Wall Magnet Orientation and Radial Position	90° ‡, 120°, 150°	3.4	Section 4.2.1
	Front-Side	Front Wall Magnet Orientation Only	30°, 60°, 90°, 120°, 150°	3.4	Section 4.2.2
	Front-Side	Radial Spacing	90°	3.7	Section 4.2.3
	Front-Back	Front Wall Magnet Radial Position	0°	3.5	Section 4.2.4
	Front-Back	Radial Spacing	0°	3.5	Section 4.2.5
	Front-Front	Radial Spacing	180°	3.8	Section 4.2.6

† survey performed by Deshpande and Menart (2004) ‡ survey performed by Deshpande et al. (2005)

Table 3.1: Ring-cusp magnet circuit configurations surveyed.

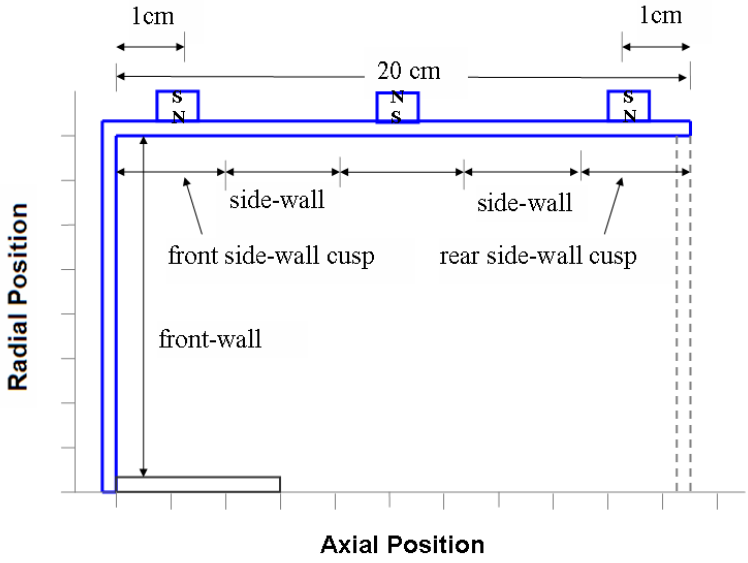

Figure 3.2: Discharge chamber with a fixed length and varying number of side wall magnet rings parallel to one another.

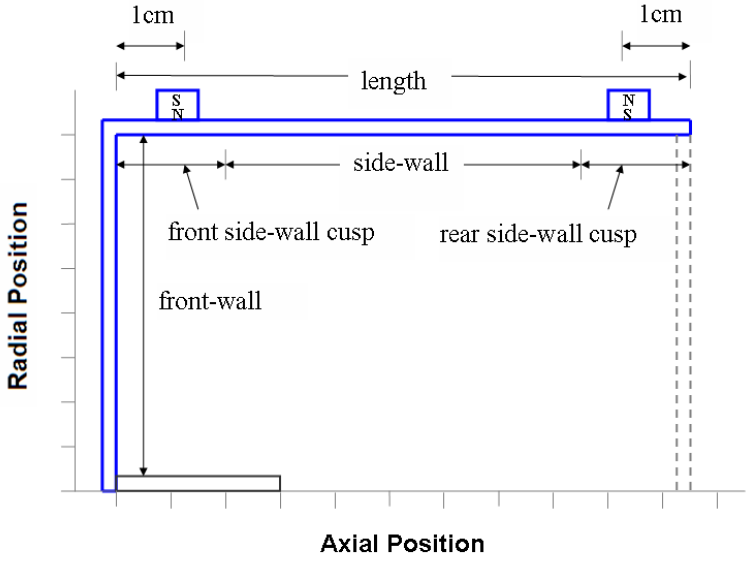

Figure 3.3: Discharge chamber with a side-side magnet pair parallel to one another.

side-side magnet pair with varying axial spacing was the next arrangement surveyed. As shown in the schematics for this configuration (Fig. 3.3), both side magnets are fixed $1cm$ from the front wall and the back wall of the chamber, and the axial spacing is varied by increasing the length of the discharge chamber.

One configuration surveyed is a front-side magnet pair with varying axial spacing as shown in the schematics of Fig. 3.4. The axial spacing is varied with the length of the discharge chamber, and the front magnet ring is positioned on the front wall $1cm$ from the axis of symmetry of the chamber, and oriented at different angles in relation to the side magnet pole. The side magnet is situated $1cm$ from the rear of the chamber. Deshpande et al (2004) surveyed the front-side magnet pair configuration with the pole axi of the magnets oriented at $90°$ (i.e. the pole of the front magnet ring is normal to the front wall). The other front magnet orientations (see Table 3.1) surveyed in this work are $120°$ and $150°$.

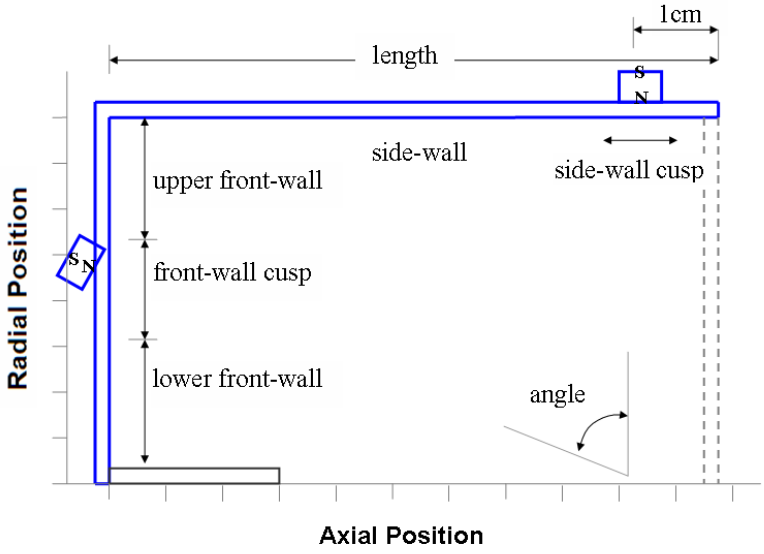

Figure 3.4: Discharge chamber with a front-side magnet pair oriented at an angle.

A front-back magnet pair, as shown in Fig. 3.5, has the back magnet centered on a $1cm$ lip at the rear of the chamber. The front magnet is positioned directly inline with the back magnet such that the magnet pole angle is $0°$. In essence, both magnets are $0.5cm$ from the side wall. In this configuration, the axial spacing is varied by the length of the chamber.

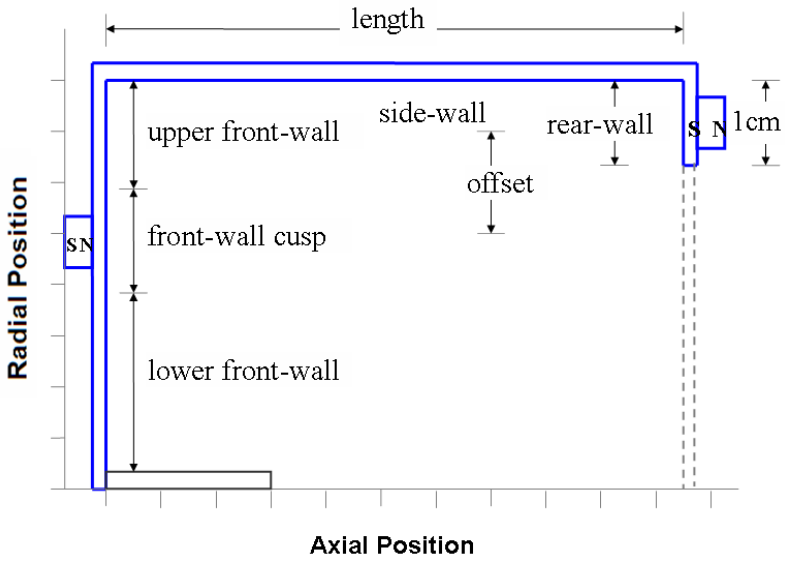

Figure 3.5: Discharge chamber with a front-back magnet pair facing each other.

A side-back magnet pair, as shown in Fig. 3.6, has a side magnet positioned $1cm$ from the front wall, and the other back magnet is centered on a $1cm$ lip at the rear of the chamber. The axial spacing between this magnet pair with a $90°$ orientation is varied by changing the length of the discharge chamber.

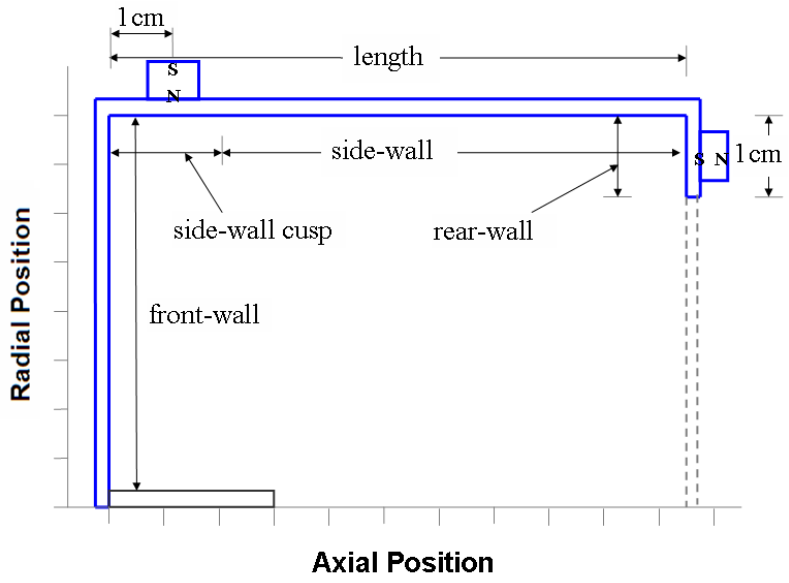

Figure 3.6: Discharge chamber with a side-back magnet pair perpendicular to one another.

3.1.2 Magnet Ring Pair with Varying Radial Spacings

The second class of configurations surveyed considers radial spacings between magnet pairs. The variation in the radial spacing is achieved by altering the diameter of the discharge chamber. Also included in this radial configuration class are surveys in which the radial position of the front magnet ring is varied while the axial spacing between the magnet pair is fixed at spacings obtained from the axial spacing studies. Table 3.1 lists the configurations in this survey class.

First in this class, a front-side magnet pair configuration with varying front magnet orientation and radial position is surveyed. In this arrangement (shown in Fig. 3.4) the front magnet ring is oriented at different angles with respect to the side magnet pole, and its radial position is varied along the chamber's front wall. The orientations considered are $90°$, $120°$ and $150°$, and the side magnet ring is positioned $1cm$ from the rear of the

discharge chamber. The front-side magnet pair configuration with the 90° oriented front magnet was surveyed by Deshpande et al. (2005). In all radial spacing surveys, the axial spacing is fixed at the predetermined value obtained from the front-side pair axial spacing survey.

A front-side magnet pair arrangement, similar to the above described configuration shown in Fig. 3.4, is used to study the effect of varying the front magnet angle. This configuration has the axial spacing between the magnet pair fixed at a spacing determined from the front-side magnet pair survey in which the axial spacing was varied. The front magnet is located at a position determined from the radial position survey of a front-side magnet pair arrangement. The front magnet ring is oriented at 30°, 60°, 90°, 120°, and 150°.

Another configuration in this radial spacing class is the front-side magnet pair which, as the notation implies, consists of one magnet ring positioned on the front wall and the other positioned on the side wall $1cm$ from the front wall as shown in Fig. 3.7. The location of the front magnet is a computed rule-of-thumb determined from the radial positioning survey of a front-side magnet pair arrangement. As both front and side magnet rings are fixed relative to the axis and front wall respectively, the radial spacing between the pair is varied by increasing the diameter of the chamber.

A front-back magnet pair with the configuration shown in Fig. 3.5, has the back magnet centered on a $1cm$ lip at the rear of the chamber, and the front magnet ring's position is varied radially. The axial spacing which remains unchanged, is obtained from the front-back magnet pair survey in which the axial spacing was varied. In essence, the axial spacing

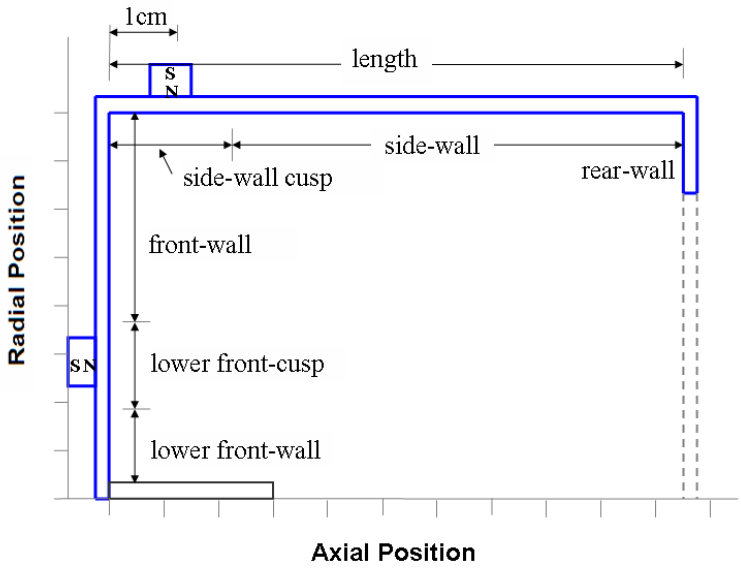

Figure 3.7: Discharge chamber with a front-side magnet pair perpendicular to one another.

from the front-back magnet pair axial survey that gave the maximum electron confinement is utilized in this survey. The angle between the magnet poles is $0°$.

A front-back magnet pair configuration (Fig. 3.5) surveys the effects of their radial spacing on primary electron confinement. Based on guidelines garnered from the front-back magnet pair survey, where the front magnet's radial location varied, the front magnet is fixed $4cm$ from the axis of the chamber. The back magnet is fixed on a $1cm$ lip at the rear of the chamber. For this configuration, the axial spacing between the magnet pair is fixed at the ideal spacing obtained from the front-back wall study in which the axial spacing is varied. The radial spacing is obtained by altering the diameter of the chamber.

A front-front magnet pair has both magnet rings positioned on the front wall of the discharge chamber. For this configuration with schematics (shown in Fig. 3.8), the lower front magnet is fixed at a specified distance from the axis of symmetry and the upper front

magnet is fixed $1cm$ from the side wall. The position of the lower front magnet is a computed guideline and its deduction is discussed in the survey results presented in the next chapter. The radial spacing between the $180°$ oriented magnet pair is varied by altering the diameter of the discharge chamber.

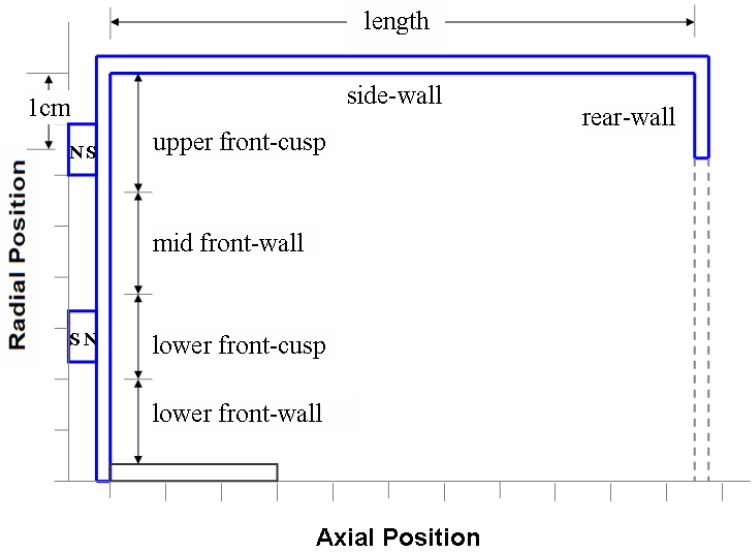

Figure 3.8: Discharge chamber with a front-front magnet pair oriented $180°$ to one another.

3.2 Geometric, Property and Operating Specifications for Surveys

For all ring-cusp magnet circuit configurations surveyed, both in this work and that by Deshpande and Menart (2004) and Deshpande et al. (2005), the material properties, discharge chamber operating parameters, and some geometric parameters remained unchanged.

These unvaried parameters also include parameters such as the magnetic field domain size, the sample size, the spatial grid size, and the time step.

For the discharge chamber, aluminum walls were used since they do not interact with the magnetic field. The selection of a $0.1cm$ thick chamber wall was based on a convergence study by Deshpande and Menart (2004) which revealed a relation between wall thickness and the absorption of electrons at the cusp region. Deshpande observed that for each study of a constant diameter chamber with magnet spacings of $3cm$, $5cm$, $11cm$, and $15cm$, the confinement length dropped by more than 50% as the wall thickness was increased from $0.05cm$ to $4cm$. Deshpande showed that as the inner surface of the absorbing chamber wall became farther from the surface of the magnet (i.e. the chambers wall thickness was increased), the cusp region becomes a weaker reflector for particles as the shape of the magnetic field at the cusp becomes more spread out. Thinner chamber walls are better, but a $0.1cm$ wall thickness is used in this work.

Rare earth samarium cobalt magnets with a residual magnetic field of $10,000gauss$, and a coercive force of $-9300oersteds$ provide the magnetic fields. The permanent magnets are $0.635cm$ wide and $0.475cm$ thick in the normal direction to the wall on which they are situated.

The operating specifications utilized for all surveys are tabulated in Table 3.2. An important note not listed, is the cathode emission point of the primary electrons. The emission location was fixed on the centerline at $3cm$ from the front wall on the axis of symmetry of the chamber. For the fixed chamber length survey performed by Deshpande et al. (2005), the emission location of the primary electron is at the center of the chambers

front wall.

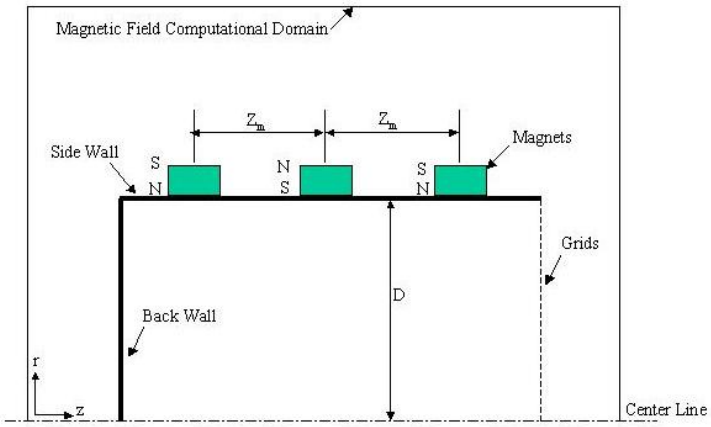

Figure 3.9: Convergence studies computational model (Deshpande, 2004).

Other parameters that remain unchanged are the magnetic field domain size relative to the primary electron domain size, the primary electron sample size, the spatial grid size, and the time step (tabulated in Table 3.2).

The magnetic field computational domain used in MAXWELL 2D was selected by Deshpande and Menart (2004) based on the magnetic flux induction field values determined by a convergence study. The domain, as shown in Fig. 3.9, required the computational boundary conditions located infinitely far from the chamber walls. In three setups where the selected magnetic field computational domain was $5cm$, $10cm$, and $15cm$ larger than the primary electron computational domain, the magnetic flux density did not change for magnetic computational domains more than $10cm$ out from the primary electron computational domain. As such the radial and axial distances of the magnetic field computational

Operating Specifications	
Discharge voltage (V_d)	30 eV
Input electron temperature	5 eV
Propellant	Xenon
Propellant mass flow rate ($\dot{m}_p$)	0.2 amp-eq
Propellant Utilization Efficiency (η)	0.8
Beam diameter	10 cm
Grid Transparency to neutral atoms (ϕ_n)	0.10
Grid transparency to ions (ϕ_i)	0.40
Neutral number density	5.5 $\times 10^{12}$cm^{-3}
Ion number density	4.9 $\times 10^{11}$cm^{-3}
Magnetic field domain size	+ 10 cm
Sample size (N)	5000 electrons
Spatial grid size (Δx)	0.02 cm
Input numerical time-step (Δt^*_{input})	0.001
Lower time step ($\Delta t^*_{cut-off}$)	5.0 $\times 10^5$

Table 3.2: Operating and numerical parameter specifications for computational surveys.

domain was set at $10cm$ from the electron computational domain.

Convergence studies for PRIMA performed by Mahalingam and Menart (2002) give the numerical parameters in MAXWELL 2D and PRIMA (see Chapter 2 Section 2.2.4 on page 24). For these numerical parameters, the confinement length is used to determine convergence. Since the numerical convergence of one parameter is dependent on the others, the convergence investigation is done iteratively. The numerical parameters converged are the sample size, the spatial grid size, and the time step.

Mahalingam's (2002) sample size convergence study showed that convergence of the confinement length within 2% was achieved with 2000 particles. Conversely, a larger sample size was necessary to obtain a reasonable particle number density distributions. Given the statistical inaccuracy of a small sample size and the long computational time of a large sample size, a medial 5000 particles are emitted and tracked for all the surveys in this study.

In MAXWELL 2D, the magnetic vector potential, A_θ^*, is exported to PRIMA as values at the nodes on the square grids used to discretize the magnetic field computational domain. Since the grid size used affects the accuracy of the results computed by PRIMA, a grid size convergence study by Deshpande and Menart (2004) shows that for a fixed case, the confinement length stabilizes for grid sizes less than $0.05cm$. Since the grid size does not strongly affect computational time, to increase the accuracy of the results from PRIMA, a $0.02cm$ grid size is used in all surveys in this work.

Mahalingam (2002) observed that the confinement length remained fairly flat for varying upper limit on the nondimensional time steps. The timestep used in PRIMA is automatically varied between an input upper and lower limit base on the strength of the magnet

field at a given location in the discharge chamber. Despite a slight oscillation for the time increment from 0.005 to 0.01, there was only a 0.7% change in the confinement length between a 0.001 and 0.00005 time step. There is only a weak dependence of the confinement length on this upper limit of the time step. As such, a 0.001 nondimensional time step was used in the Runge-Kutta numerical scheme (see Section 2.2.4). For the minimum time step, Mahalingam selected 5×10^{-5} for the following reasons. For highly-curved paths (i.e. small Larmor radii) of the primary electrons, the time step limit was required to be small enough to accurately follow the curvature of the electron's trajectory, but high enough to attain reasonable computational times. In addition, for a lower limit on the time steps of 5×10^{-5}, 10% of the particles tracked deviate from the realistic nondimensional particle velocity range of 1.0.

3.3 Primary Electron Absorption Mechanisms

For the surveys presented in this work, the primary electron confinement length is the parameter used to determine the performance of a discharge chamber with a given magnet circuit configuration. Since increased ion confinement translates to increased propellant ionization and thus increased ion thruster performance, a long confinement length that permits stable operation is preferred. Based on observations of the results from previous configurations and those included herein, the confinement length is affected by two primary mechanisms corresponding to the areas where primary electrons are absorbed at the walls. Confinement lengths are influenced by the magnetic field shape at the cusps and the strength of the magnetic field between adjacent magnet rings.

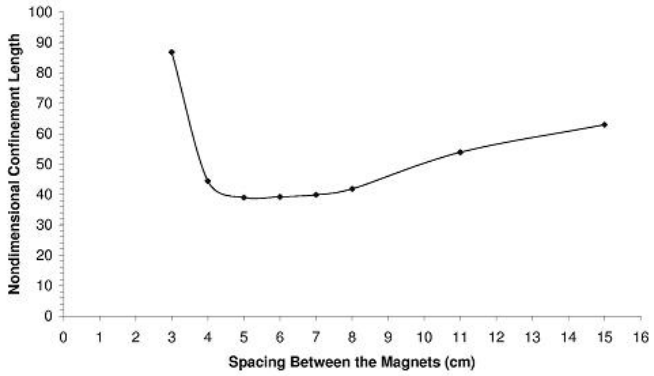

Figure 3.10: Effect of spacing between the magnets on the nondimensional confinement length (Deshpande and Menart, 2004.

The cusp is defined as the region where magnetic field lines terminate at the magnet pole. Previous studies by Deshpande and Menart (2004) have shown the effect of the cusp magnetic field shape on confinement. In his cusp region study, a $4cm \times 5cm$ primary electron computational domain was centered on a central magnet cusp whose shape was altered by the spacing of adjacent magnets on either side. As the magnetic field shape at the cusps was varied by increasing the spacing of the adjacent magnets, the nondimensional confinement length initially decreased before eventually increasing as shown in Fig. 3.10. Given the small $4cm$ axial length of the domain in Deshpande and Menart's study, the electron absorption mechanism at the cusp was adequately isolated; all cusp shapes studied had an average of only 0.86% of the $20,000$ electrons absorbed outside the cusp. The low confinement length for intermediate magnet spacings (as observed in Fig. 3.10) illustrates

increased absorption at the cusp due to a favorable magnetic field cusp shape. Deshpande and Menart postulated that the higher confinement length at smaller magnet spacings illustrates the increased mirroring ability of the cusp due to the shape of the magnetic field at the cusp. In essence, the results obtained demonstrated that the cusps are a major factor affecting electron absorption at the anode discharge chamber walls. In a study of the effect of the wall thickness on electron confinement, briefly covered in the preceding section (Section 3.2), Deshpande and Menart further confirm the relation between the cusp and electron confinement.

Also observable in this work, are the cusp-effect at the virtual cusp formed at the front wall at the base of the cathode. For a front magnet ring, magnetic field lines closer to the axis of the chamber originate and terminate at the north and south pole of the front magnet ring respectively (see Fig. 3.1). Consequently, in the lower front wall region, just around the base of the cathode, the field lines run normal to the wall thereby creating a virtual cusp that acts to decrease the confinement length as electrons easily reach the anode-biased wall. The shape of this cusp is altered by the diameter of the front magnet ring and the surface area covered by the cathode.

Deshpande and Menart's cusps region study also depicts the effect of the strength of the magnetic field on confinement. For large spacings between adjacent magnets, Deshpande and Menart's (2004) cusps region study shows an increase in the particles absorbed outside the cusps. This absorption occurs at the location between adjacent magnet rings, because of the weakness in the field far away from the magnets. In essence, a hole in the magnetic field occurs for adjacent magnets placed too far apart. Both primary electron

absorption mechanisms are further observed in the proceeding surveys.

4. Results of Magnet Circuit Configuration Survey

The results of the various ring-cusp magnet circuit configurations discussed in the previous chapter are presented here. The results of the various magnet circuit configurations surveyed is classified according to the variation of either the axial or radial spacing between magnet pairs. Table 3.1 on page 32 lists the configurations in each classification and includes the sections in which the results of each configuration are discussed. The convention describing the configuration types is explained in Chapter 3 Section 3.1. The guidelines deduced from the configurations surveyed are summarized in Table 4.1. The surveys presented herein complement previous surveys by Deshpande and Menart (2004) and Deshpande et al. (2005). The survey results by Deshpande et al., and Deshpande and Menart are briefly presented in this chapter. Except for the magnet circuit configuration that involves increasing the number of magnets on a fixed length discharge chamber, all other configurations focus on determining general guidelines applicable to interacting magnet pairs. The objective of this approach is to ultimately apply these guidelines to more complex magnet circuit configurations on any axi-symmetric discharge chamber with walls that do not interact with the magnetic field. Complex magnet circuit configurations are presented in the next chapter.

4.1 Axial Spacings

4.1.1 Fixed Length Chamber with Varying Number of Side Wall Magnet Rings

Deshpande and Menart (2004) investigated a magnet circuit configuration where only side magnet rings are placed on the discharge chamber as shown in Fig. 3.2. The objective was to determine the axial spacing between parallel magnets ($180°$) that provided maximum primary electron confinement. To vary the axial spacing between adjacent magnet rings on a $20cm$ fixed-length chamber, the number of side magnet rings was varied such that with two magnet rings the spacing was $18cm$ and with three magnet rings the axial spacing was $9cm$. For various chamber radii, Deshpande and Menart's plot (Fig. 4.1) showed that increasing the number of magnet rings initially increased the confinement length before it eventually decreased as more magnet rings were introduced. The best spacing between adjacent magnet rings occurred between $9cm$ and $18cm$. The trend observed in the plot indicates that more magnet rings are not always better. As discussed in the previous chapter in Section 3.3, two alternating and competing mechanisms contribute to low primary electron lengths. These competing mechanisms are the primary electron absorption at the cusps, and primary electron absorption at the weakly protected walls between the cusps. In essence, lower confinement lengths for small axial spacings (high number of magnets) resulted from electron absorption at the increased number of cusps. Conversely, the lower confinement lengths for large axial spacings (low number of magnets) resulted from increased electron absorption at the hole in the weakening magnetic field between the cusps.

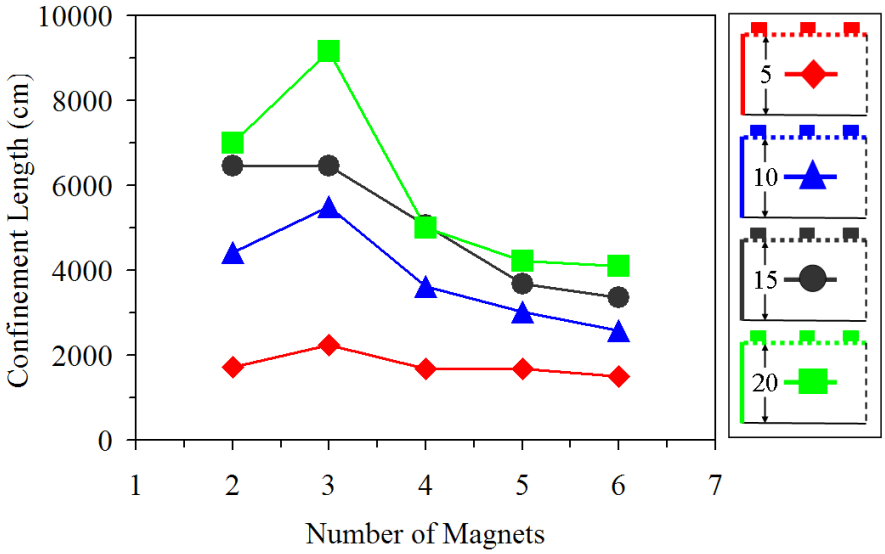

Figure 4.1: Confinement length as a function of the number of side magnet rings on a $20cm$ fixed-length chamber.

In summary, the results of Deshpande and Menart (2005) survey showed that the spacing between magnet pairs can be optimized for maximum electron confinement.

4.1.2 Side-Side Pair with Varying Axial Spacing

The side-side magnet pair configuration studied by Deshpande and Menart (2004) and shown in Fig. 3.3, refined the fixed length chamber with varying number of magnets. The varying number of magnets survey (see Section 4.1.1) concluded that the optimum axial spacing between magnets occurs between $9cm$ and $18cm$. To further narrow this range, a similar survey had only two magnet rings positioned on the side walls of the chamber. Deshpande et al. varied the axial spacing between the magnet pair by altering the length of the chamber. A plot of the confinement length as a function of the spacing between

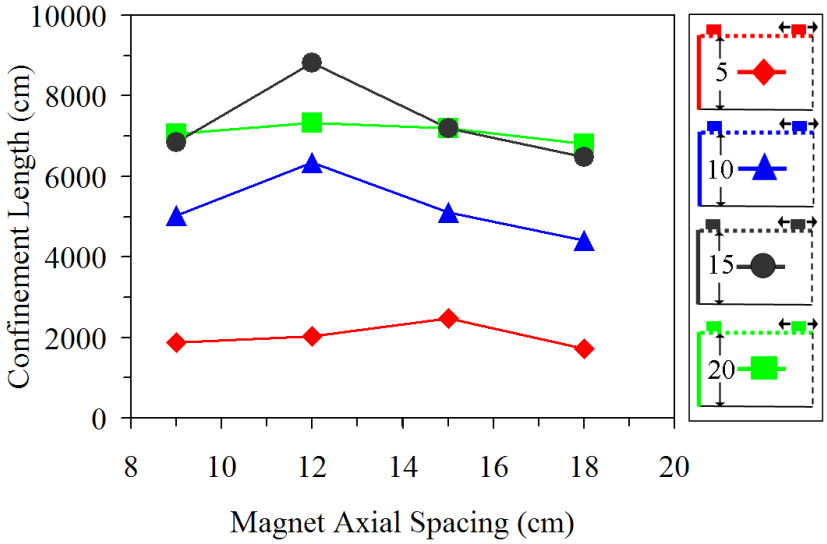

Figure 4.2: Confinement length as a function of the axial spacing between a side-side magnet pair.

the magnet pair (Fig. 4.2) showed that for most chamber radii the maximum confinement length invariantly occurred at a $12cm$ axial spacing. Although, the $5cm$ radius discharge chamber resulted in a peak at $15cm$, given its close proximity to the other results, it was concluded that for any discharge chamber diameter the optimum axial spacing should occur between $12cm$ and $15cm$.

4.1.3 Front-Side Pair with Varying Front Wall Magnet Orientation and Axial Spacing

Plotted in Fig. 4.3 and Fig. 4.4 are the results of a survey for a $5cm$ and $10cm$ radius chamber respectively. The axial spacing of a front-side magnet pair is varied by increasing the length of the discharge chamber. For this configuration (Fig. 3.4), the front magnet is

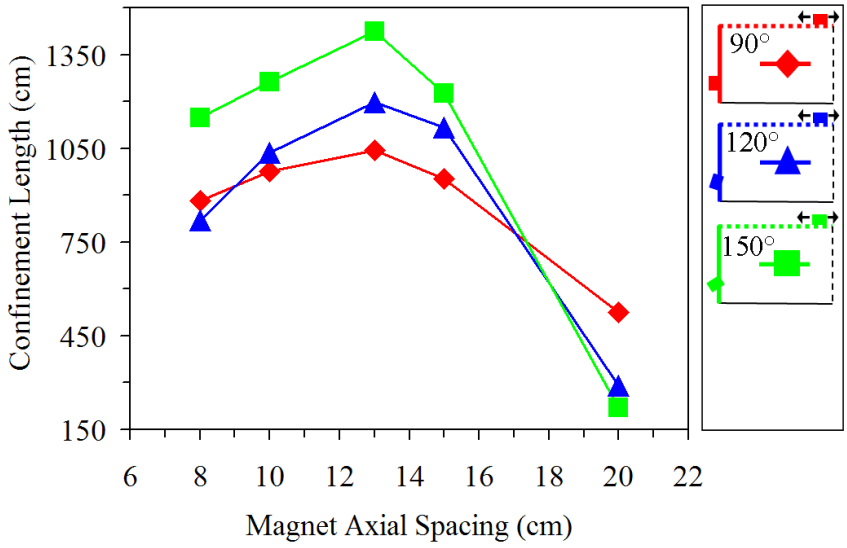

Figure 4.3: Confinement length as a function of the axial spacing between a front-side magnet pair on a $5cm$ radius chamber.

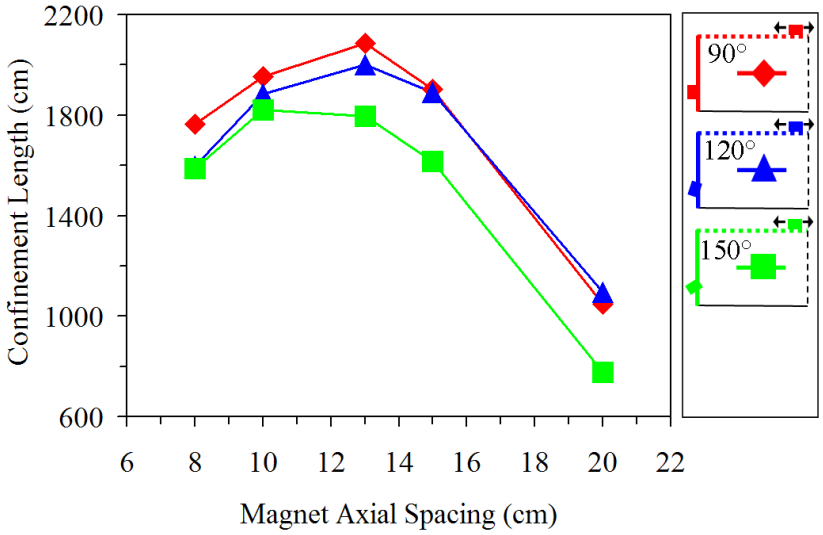

Figure 4.4: Confinement length as a function of the axial spacing between a front-side magnet pair on a $10cm$ radius chamber.

oriented at different angles (listed in Table 3.1) and fixed $1cm$ from the axis of the chamber. All walls of the chamber are set to absorb electrons.

Deshpande et al. (2005) surveyed the front-side magnet pair configuration with the front magnet flushed ($90°$) with the front wall. In that survey by Deshpande et al., for the $5cm$ and $10cm$ radii chamber (Fig. 4.3 and 4.4 respectively), the best electron containment occurred when the axial spacing between the magnet pair was $13cm$. This $13cm$ optimum axial spacing is reasonable as it falls within the $12cm$ and $15cm$ range established for the side-side parallel oriented magnets surveyed by Deshpande et al. (2005).

When the front magnet is oriented at $120°$ and $150°$, results like Deshpande et al.'s $90°$ orientation survey are obtained. In the $5cm$ radius chamber survey (Fig. 4.3), the maximum confinement length occurs when the axial spacing between magnets is $13cm$. For a $10cm$ radius chamber survey (Fig. 4.4), maximum confinement of the $120°$ case occurs at $13cm$ while the $150°$ case gives a maximum at $10cm$. However, finer resolution in the results would probably indicate this maximum is closer to $13cm$.

The lower confinement lengths that occur at close and far axial spacings, result from the competing electron absorption mechanisms (see Chapter 3 Section 3.3) that are observed in the plot of the percentage of particles absorbed at the chamber walls (Fig. 4.5). In this flux plot for a $10cm$ radius chamber with a $120°$ oriented front magnet ring, at close axial spacings the primary electron absorption at the lower front wall and side wall are low and the flux through the side and front cusps dominate. As the axial spacing increases, absorption at the cusps decrease while absorption to the side wall steeply increases. The increasing electron absorption at the side wall is verifiable from the relative number density

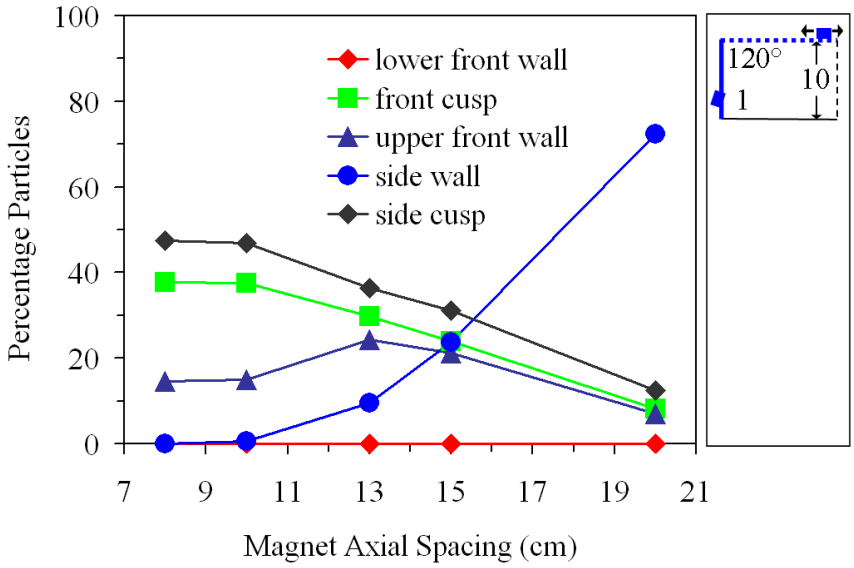

Figure 4.5: Percentage of particles absorbed as a function of the axial spacing between a front-side magnet pair.

plot (Fig. 4.6) which shows the 1×10^{-6} contour line increasingly exposed to the side wall as the axial spacing increases. Since the contours in the relative number density plot indicate the number of the particles present at a given point, the increased exposure of the 1×10^{-6} contour line to the wall indicate that a higher number of the primary electrons contact the wall at this location. The reason for the increase in the number of particle expediently reaching the side wall is seen in a magnetic vector potential plot (Fig. 4.6). Noticeable, is the increasing spacing between strong magnetic field lines (like the $50 gauss\text{-}cm$) as the magnet spacing is increased. These developing areas of weak magnetic fields (areas where the magnetic field lines do not run across the wall) allows increased electron absorption at these points. Figure 4.5 clearly points out that the trade-off between absorption at the cusp or wall occurs at the intermediate spacing where the curves intersect. Although this occurs

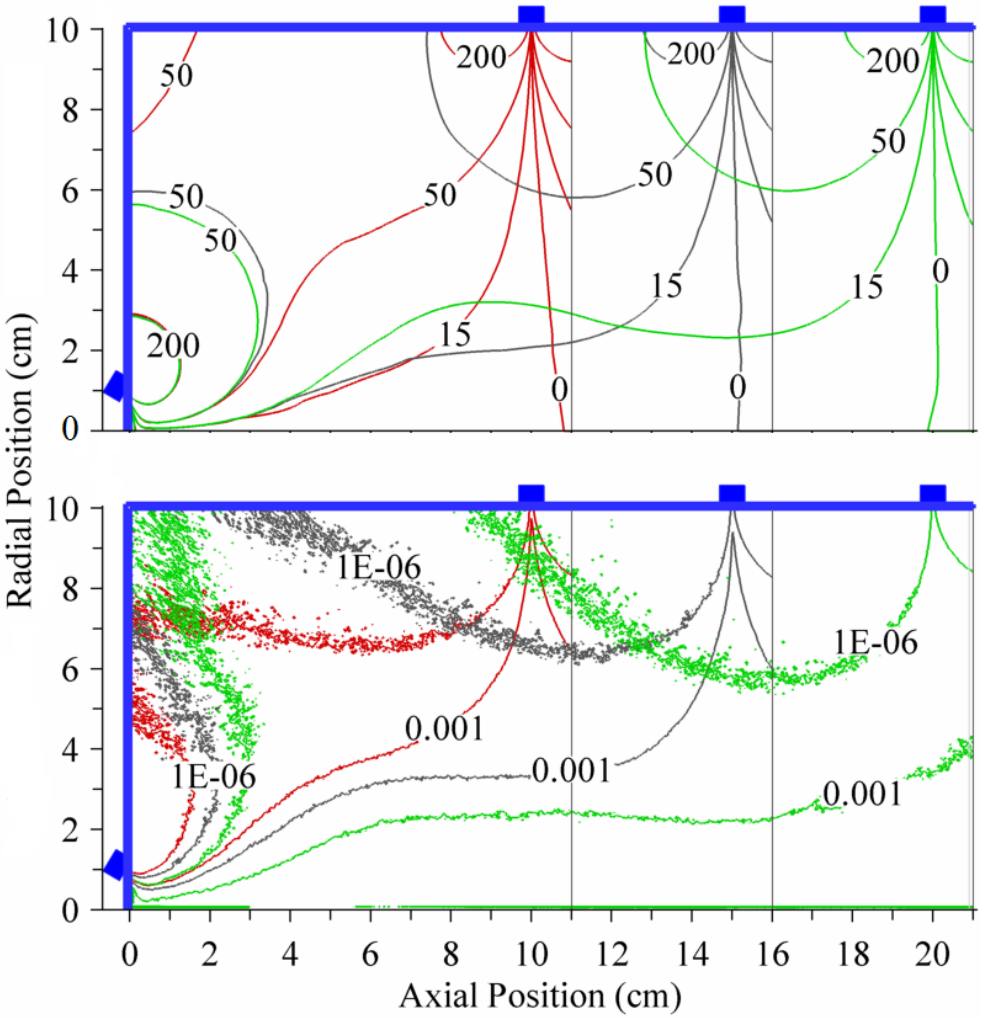

Figure 4.6: Magnetic vector potential contours (in gauss-cm) and relative number density contours for a front-side magnet pair with varying axial spacing and a $120°$ oriented front magnet.

at a slightly higher spacing than the optimum at $13cm$, it is still very close to this value.

It is conclusive from this front-side magnet survey, that a favorable axial spacing of $13cm$ is essentially independent of the orientation of the front magnet ring and the diameter of the chamber up to $40cm$. For diameter chambers larger than $40cm$, it must be realized

that an additional magnet ring on the front wall is required to obtain maximum confinement.

4.1.4 Front-Back Pair with Varying Axial Spacing

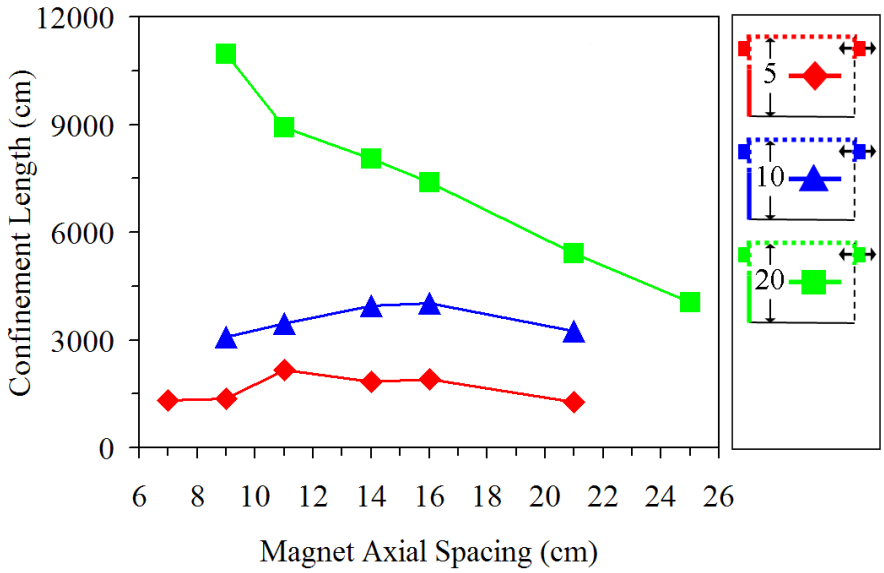

Figure 4.7: Confinement length as a function of the axial spacing between a front-back magnet pair with no radial offset.

The front-back magnet pair configuration shown in Fig. 3.5 has the axial spacing between the magnet pair varied with the length of the chamber. There is no offset between the magnet pairs which are both positioned $0.5cm$ from the side wall. To isolate the effect of the axial spacing on the primary electron confinement length, the lower front wall region of the chamber is set to reflect electrons. Fig. 4.7 shows that a $10cm$ radius discharge chamber provides maximum electron confinement when the separation between the magnets is $16cm$. The validity of this result is seen in Fig. 4.8 where at about a $16cm$ axial spacing, the electron absorption at the two cusp regions is equivalent to absorption at the side wall.

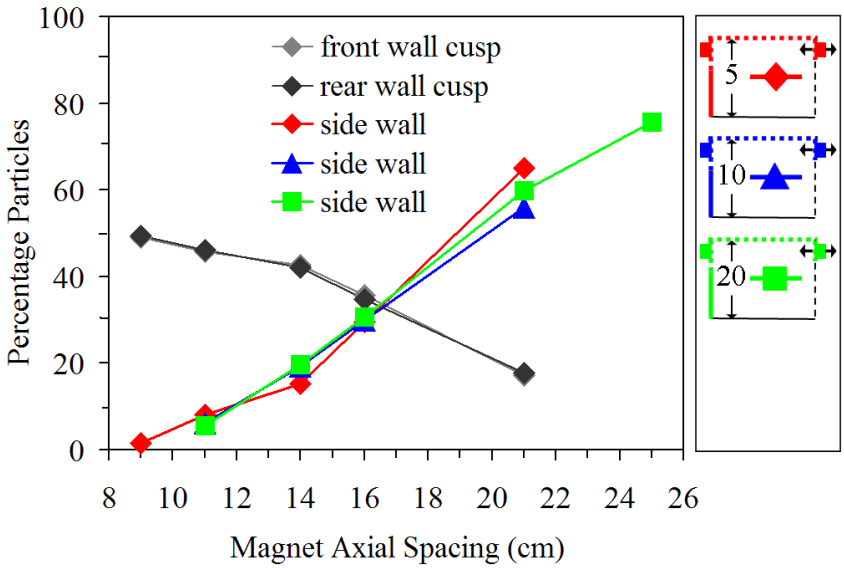

Figure 4.8: Percentage of particles absorbed as a function of the axial spacing between a front-back magnet pair with no radial offset.

Although Fig. 4.7 shows that the $5cm$ and $20cm$ radii chambers do not give maximum confinement at $16cm$, their particle fluxes shown in Fig. 4.8 are identical to the $10cm$ radius chamber. Therefore, it is concluded that their maximum confinement also occurs at about $16cm$ despite the perturbations. These perturbations are caused by the changing aspect ratio of the chamber. For instance, the confinement length for the $20cm$ radius chamber continually increases as the separation between the magnets decreases because as shown in the trajectory plot in Fig. 4.9, the radius becomes much larger than the length of the chamber and the cusps are increasingly shielded from electrons due to the pinch by strong magnetic field lines (see the $50gauss\text{-}cm$ field line). Since the walls are adequately protected by strong magnetic field lines and the cusps are shielded by the pinch, the bulk of the electrons are trapped in the middle of the discharge chamber where bounce repeatedly

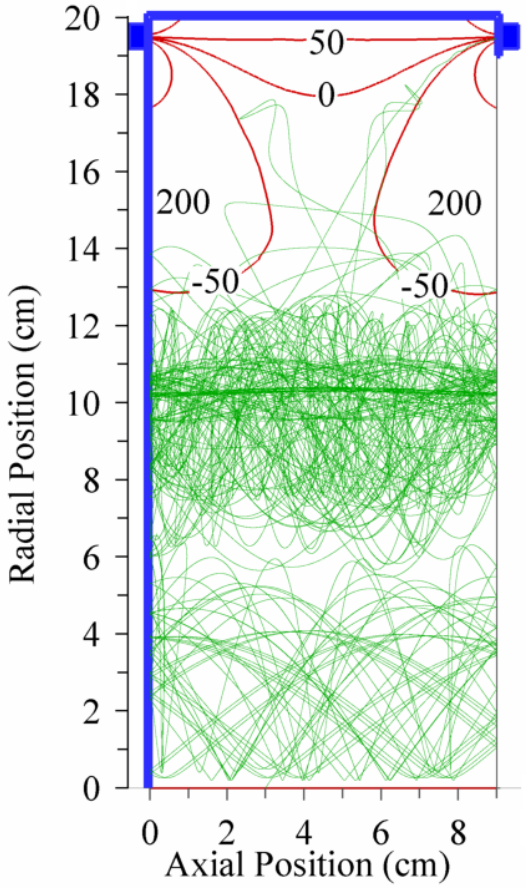

Figure 4.9: Trajectory plot of a trapped electron resulting from the skewed aspect ratio of a chamber with a front-back magnet pair.

between the reflective front wall and the grid. There are 1057 wall reflections of primary electrons for the $20cm$ case shown in Fig. 4.9 as compared to 241 and 60 for the $5cm$ and $10cm$ radius chambers respectively with similar axial spacings. A future study will have to address the effect of a discharge chamber's aspect ratio on electron confinement.

The contour plots for a $10cm$ radius chamber with a front-back magnet pair (Fig. 4.10) illustrate the low confinement length resulting from competing electron absorption at the cusps or the walls. In the number density contour plots, as the distance between the mag-

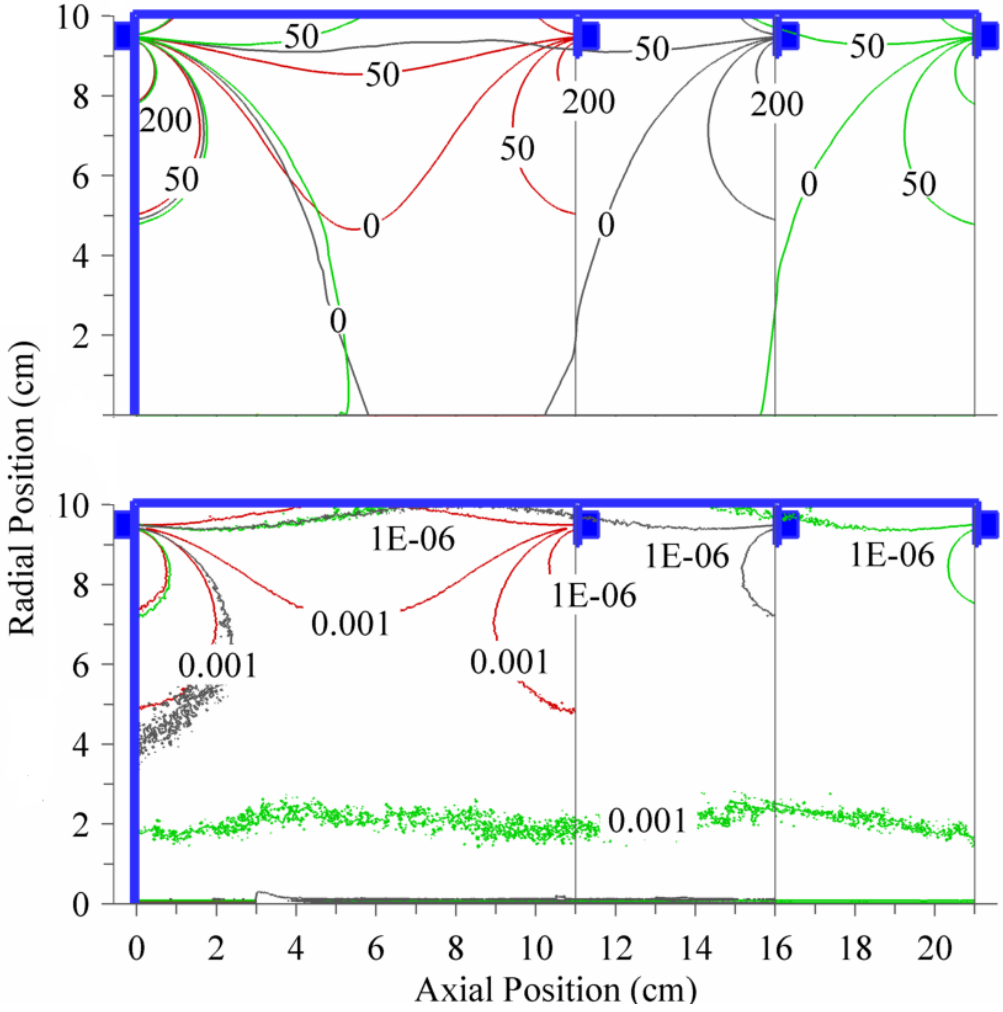

Figure 4.10: Magnetic vector potential contours (in gauss-cm) and relative number density contours for a front-back magnet pair with varying axial spacing and no radial offset between magnets.

nets increases, the 1×10^{-6} contour intersects more of the wall at the intermediate region between the magnet pair. This increase in the percentage of particles exposed to the wall corresponds to a hole formed by the decreased strength of the magnetic field at intermediate regions. As seen in the magnetic vector potential plot, the $50 gauss\text{-}cm$ magnetic field

line moves closer to the wall as the distance between the magnets increases. In contrast, as the distance between the magnets decreases, most particles are absorbed at the cusps.

In summary, to protect the side wall of a chamber and enhance maximum electron confinement, the axial spacing between a front-back magnet pair should be between $11cm$ and $16cm$, irrespective of the discharge chamber diameter.

4.1.5 Side-Back Pair with Varying Axial Spacing

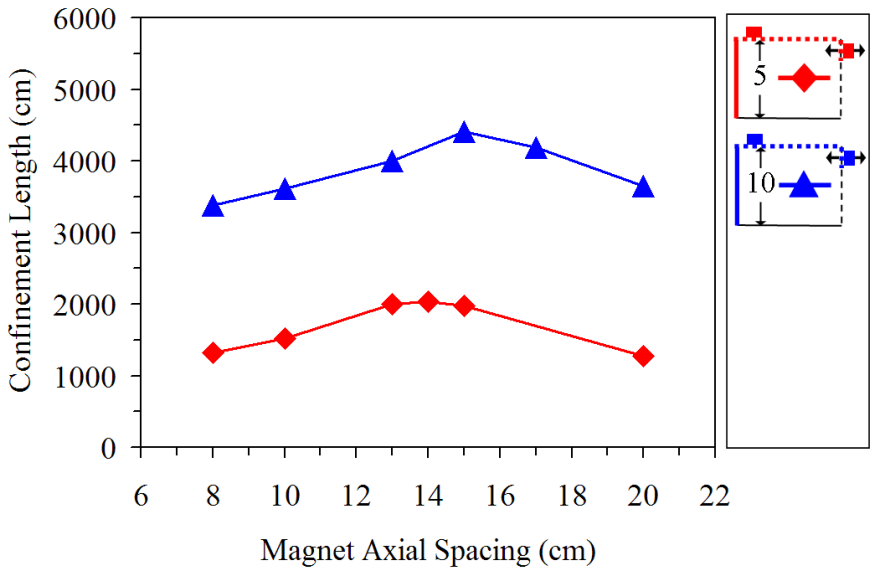

Figure 4.11: Confinement length as a function of the axial spacing between a side-back magnet pair.

In this survey, the side-back magnet pair configuration shown in Fig. 3.6, has the axial spacing by varying the length of the discharge chamber. For two chamber radii surveyed, the effect of the axial spacing on the primary electron confinement length is isolated by setting the front wall to reflect electrons. The plot of confinement length as a function of

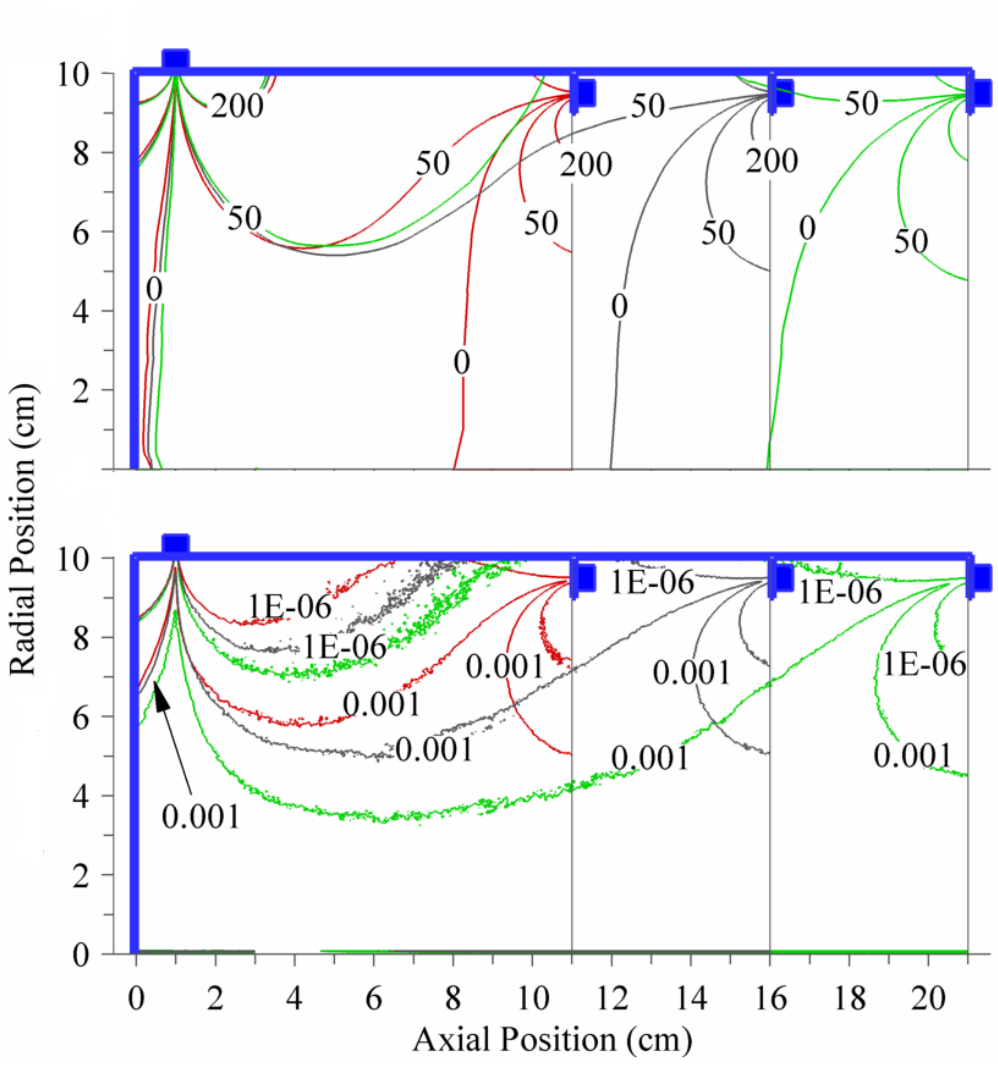

Figure 4.12: Magnetic vector potential contours (in gauss-cm) and relative number density contours for a side-back magnet pair with varying axial spacing.

the axial spacing of the magnet pair (Fig. 4.11) shows that maximum containment occurs between $14cm$ and $15cm$.

The confinement lengths decrease for close and far axial spacings because of the respective high primary electron absorption at the cusps or at holes formed in the magnetic field as the the spacing between the magnets becomes large. As shown in Fig. 4.12, the de-

veloping hole allows more electrons to reach the mid-region of the side wall where strong magnetic field lines, like the $50 gauss\text{-}cm$ line, no longer run within the chamber when the axial spacing is large. The front-side magnet pair survey of Section 4.1.3 is like the side-back magnet pair. As such it is reasonable that maximum confinement should be obtained at about the same axial spacings. The optimum axial separation for the front-side magnet pair configuration is $13cm$, and its deviation from the side-back magnet pair optimum is due to the radial location of the back and front magnets.

In summary, it is conclusive that the optimal axial spacing between a side-back magnet pair should be between $14cm$ and $15cm$. Although the optimal spacing for both chamber radii surveyed are slightly different, it is not expected that there will be any significant change in the optimal axial spacing for other chamber radii.

4.2 Radial Spacings

4.2.1 Front-Side Pair with Varying Front Wall Magnet Orientation and Radial Position

To determine the best radial position of the front magnet in a front-side magnet pair configuration (Fig. 3.4), a front magnet oriented at various angles with respect to the side magnet is studied as a function of the radial position while its axial spacing from the side magnet is maintained at the optimal $13cm$ derived from the front-side magnet pair axial spacing survey (Section 4.1.3).

Deshpande et al. (2005) performed the front-side magnet pair configuration survey with the front magnet oriented at $90°$ (i.e. the pole of the front magnet was normal to the front wall). Plots (Figs. 4.14 and 4.15) of the confinement lengths as a function of the radial position of front magnet orientations of $90°$, $120°$, $150°$ on $10cm$ and $20cm$ radii chambers show the effect of radial position. The front magnet was varied while its axial spacing from the side magnet was maintained at $13cm$. In Fig. 4.13, only the $90°$ orientation is plotted for various chamber radii. Although there is a slight variance in the radial positions that provides optimal electron confinement for the different chamber radii, the initial assumption that the front magnet should be located about halfway between the chamber axis and side wall proved incorrect. In actuality, the optimal radial location remains fixed between $3cm$ to $4cm$ from the chamber axis, irrespective of the chamber

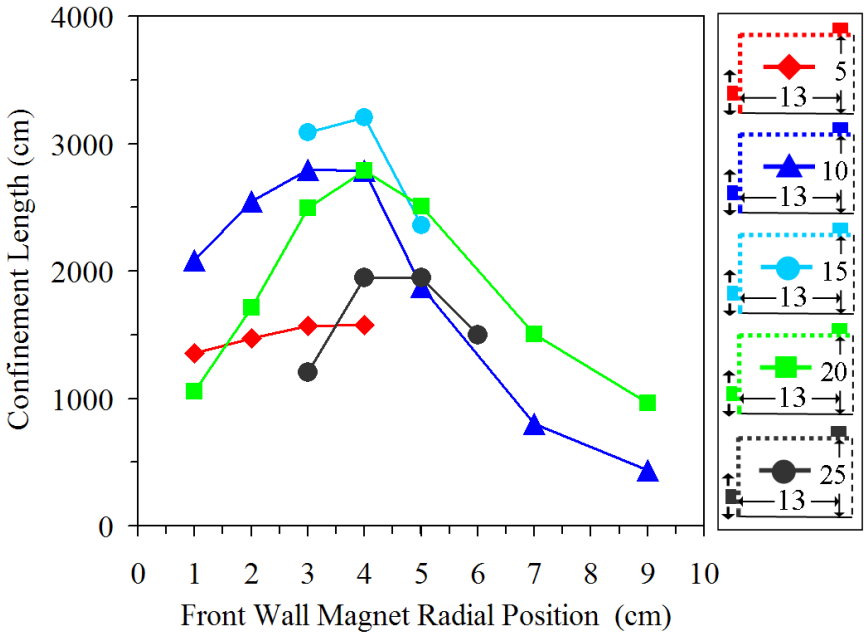

Figure 4.13: Confinement length as a function of the radial position of a $90°$ front magnet for a front-side magnet pair.

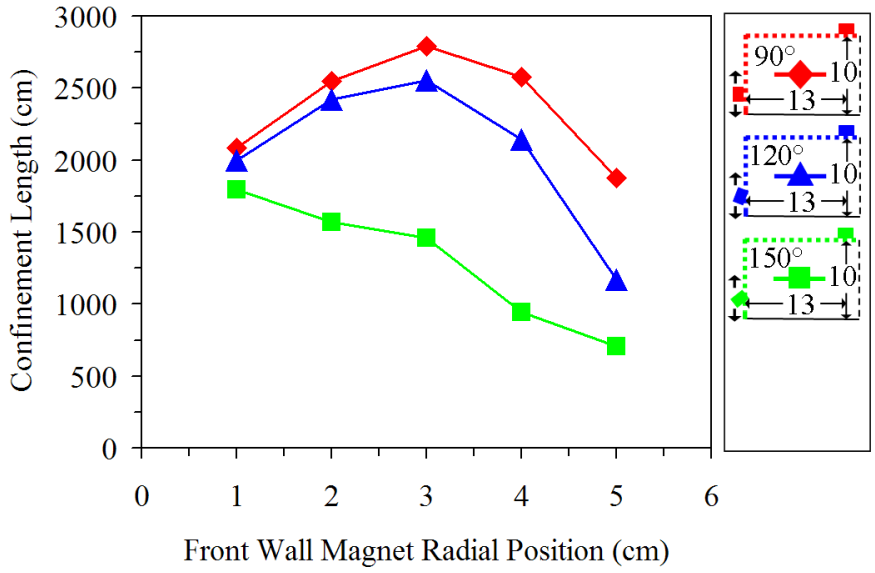

Figure 4.14: Confinement length as a function of the radial position of the front magnet for a front-side magnet pair on a $10cm$ radius chamber.

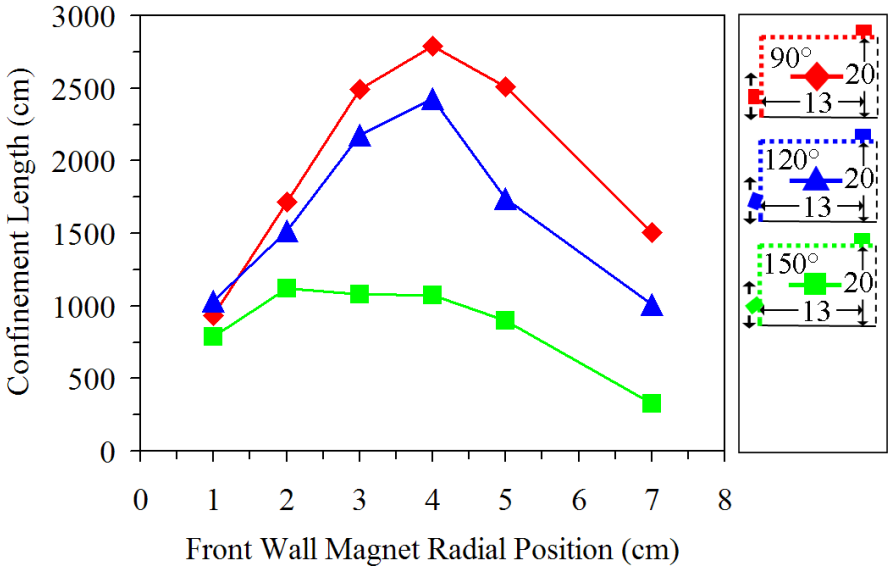

Figure 4.15: Confinement length as a function of the radial position of the front magnet for a front-side magnet pair on a $20cm$ radius chamber.

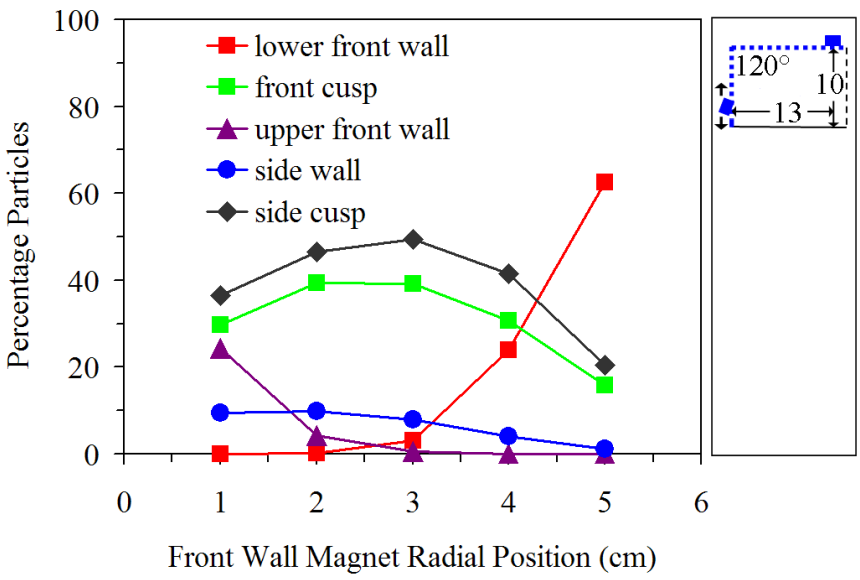

Figure 4.16: Percentage of particles absorbed as a function of the radial position of a 120° oriented front magnet for a front-side magnet pair.

radius. The validity of this guideline is evident in the all surveys in which the radial position of the front magnet is varied, like the front-back magnet pair configuration (Section 4.2.4).

The optimum radial position of the front magnet remains between $3cm$ to $4cm$ even when its orientation is varied to 120° and 150° (Fig. 4.14 and 4.15). Although the 150° survey shows otherwise, this assertion is valid and will be clarified later in this section. Similar to the $10cm$ radius chamber, a $5cm$ radius chamber (plot not shown) produces maximum confinement at $3cm$ for all angle surveys.

For both the $10cm$ and $20cm$ radii chambers, the 90° and 120° surveys show lower confinement lengths for small and large radial positions of the front magnet. The curve trends are explained by Fig. 4.16 and 4.17 which respectively plot the percentage of the electrons absorbed at the walls of a chamber with a 120° and 150° angled front magnet

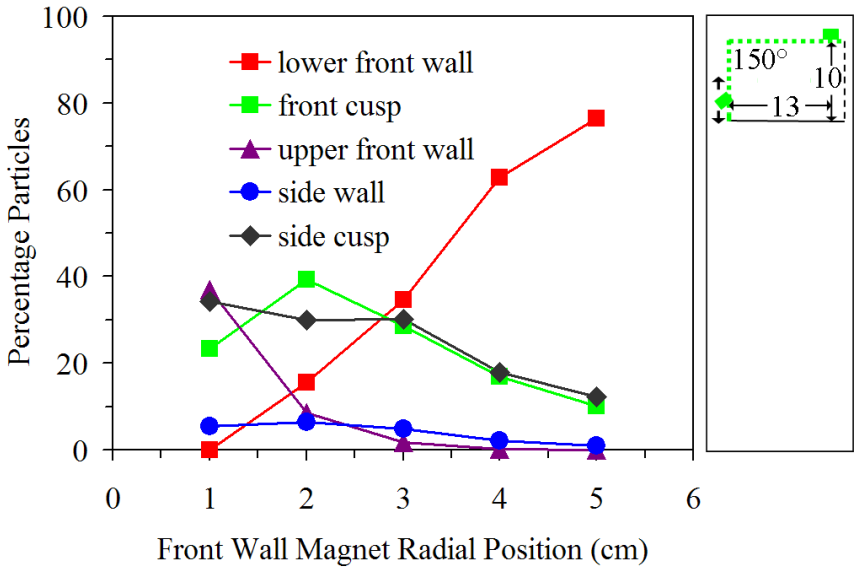

Figure 4.17: Percentage of particles absorbed as a function of the radial position of a $150°$ oriented front magnet for a front-side magnet pair.

ring. The plots show the curves of the dominant electron absorption regions, the lower front wall absorption and the cusps, intersecting each other when the front magnet is located about $3cm$ to $4cm$ from the chamber axis. The intersection of these curves illustrates that the maximum confinement occurs for a balance between the two dominant and competing electron absorption mechanisms. At small radial positions the confinement length is shorter because electrons are expediently absorbed at the cusps and at the upper front wall region which is slightly exposed because of the weak magnetic fields at this location. The weak magnetic field in this region (shown in Figs. 4.18 and 4.19) is signified by the large number of electrons contacting the wall in the corresponding relative number density plots. For large radial positions of the front magnet from the axis of symmetry, as electron absorption at the cusps remains relatively constant and absorption at the upper front wall significantly

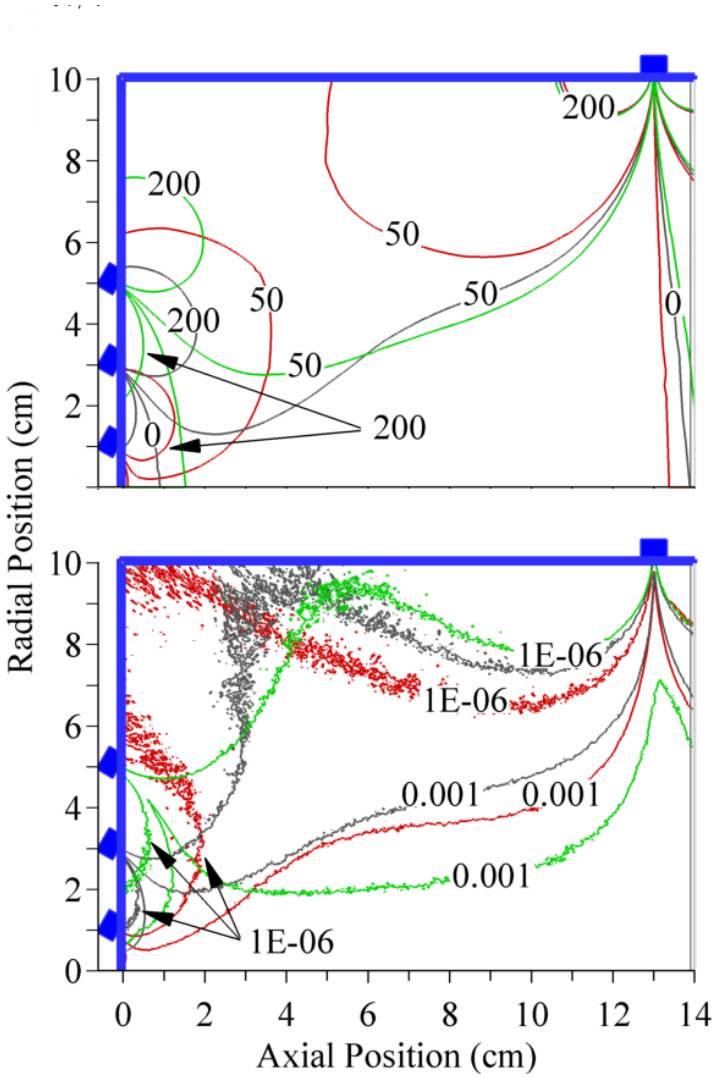

Figure 4.18: Magnetic vector potential contours (in gauss-cm) and relative number density contours for a front-side magnet pair with a varying 120° front magnet radial position.

decreases, high absorption at the lower front wall causes the short confinement lengths seen. Electron absorption at the lower front wall is more prone to proliferation as the orientation of the front magnet varies from 120° to 150°. For large angles of the front magnet (see the 150° case in Fig. 4.19) a high density of electrons (the 1×10^{-6} contour line barely runs within the chamber walls) contact the lower front wall where strong magnetic field lines

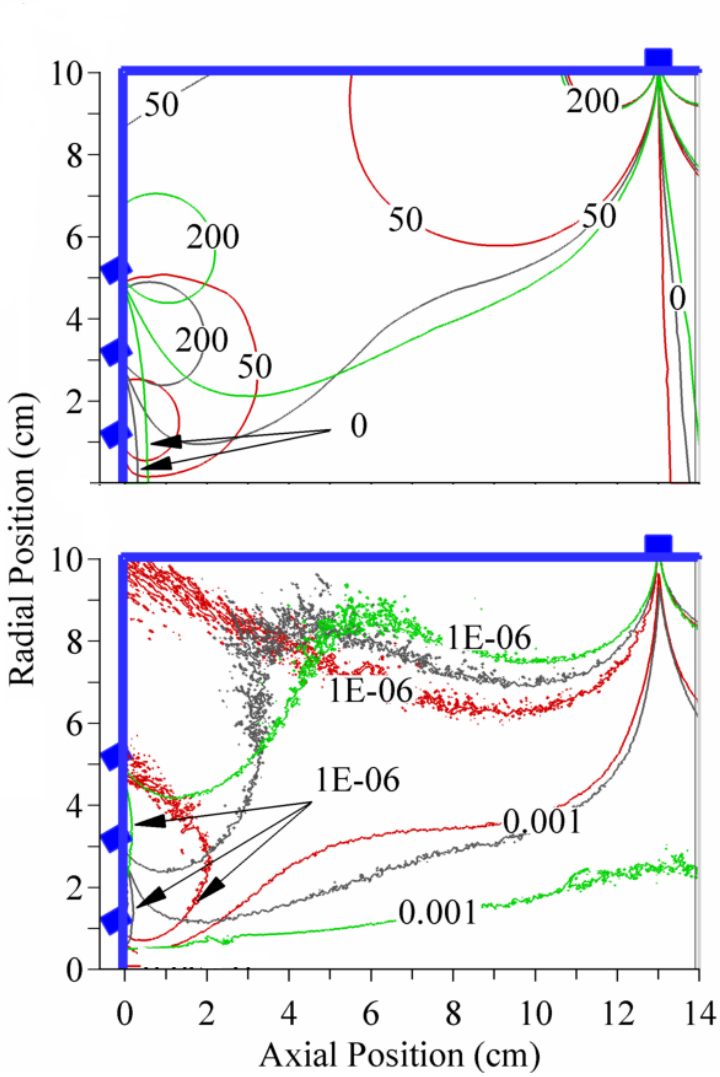

Figure 4.19: Magnetic vector potential contours (in gauss-cm) and relative number density contours for a front-side magnet pair with a varying 150° front magnet radial position.

run outside the chamber walls. For instance, the $0 gauss\text{-}cm$ field line that runs parallel and closest to the lower front wall region is an inadequate shield, hence a high particle flux is seen in this region. Furthermore, the acute angle of the front magnet is responsible for the absence of an intermediate maximum value in the 150° surveys for both chamber radii in Fig. 4.14 and 4.15. The cusp at the centerline region for the 150° front magnet

is always a problem no matter what the radial position. In summary, a front magnet ring introduces a magnetic field hole that is always present in any axi-symmetric magnet circuit configuration. It should be noted that since the cathode covers a portion of the hole that occurs at the lower front wall, its size affects the placement of the front magnet. In essence, to ensure that this field hole at the axis of symmetry is covered by the cathode, the front magnet ring should be spaced between $3cm$ and $4cm$ from the centerline of the chamber.

4.2.2 Front-Side Pair with Varying Front Wall Magnet Orientation

Another front-side magnet pair configuration survey (see Fig. 3.4) focuses on the effects of the orientation of the front magnet ring on confinement ability. For the various chamber radii surveyed, the axial spacing between the pair is fixed at $13cm$ and the front magnet is positioned $3cm$ to $4cm$ from the axis. These values are based on the guidelines obtained from other front-side magnet pair configuration surveys.

As shown in Fig. 4.20 where the orientation of the front magnet is varied, maximum confinement is independent of the chamber's radius and it occurs when the pole of the front magnet is at $90°$ and normal to the front wall. At acute angles (angles less than $90°$) and obtuse angles (angles greater than $90°$) of the front magnet ring, the confinement lengths decrease due to changing primary electron absorption at the cusps or the chamber walls. In the absorption plot in Fig. 4.21, electron absorption at the walls is largely responsible for the low confinement lengths seen for acute and obtuse front magnet orientations. At acute angles, electron absorption remains relatively equal at the cusps. The magnetic vector potential plot in Fig. 4.22 shows that holes occur at both the upper and lower front wall

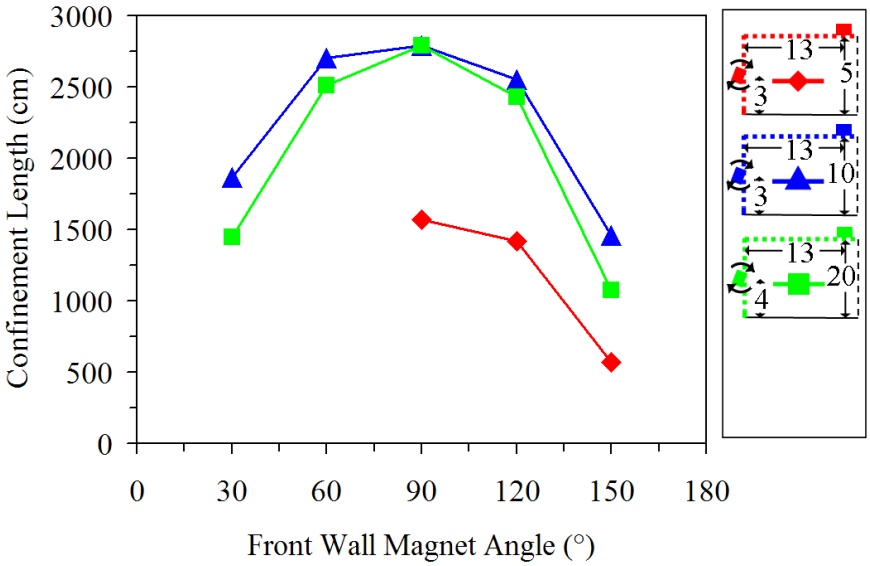

Figure 4.20: Confinement length as a function of the orientation of the front magnet on a front-side magnet pair.

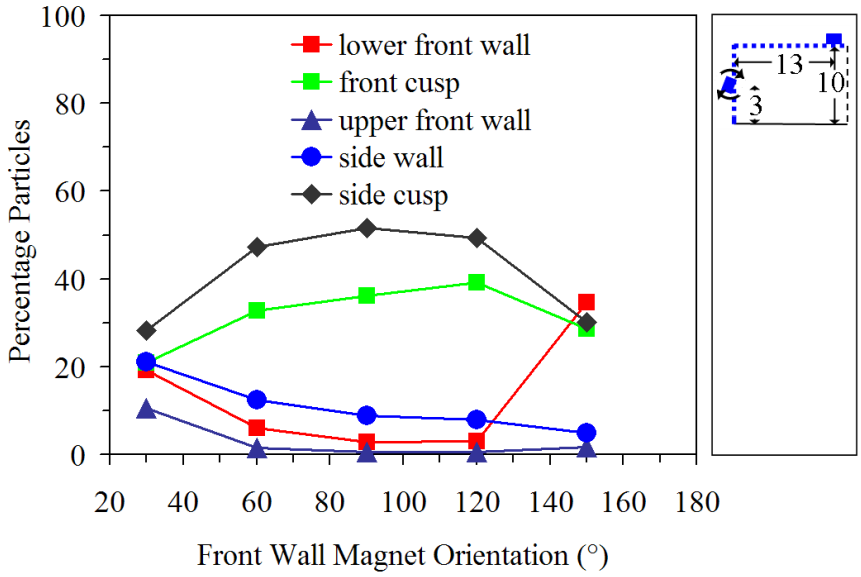

Figure 4.21: Percentage of particles absorbed as a function of varying the front magnet orientation for a front-side magnet pair.

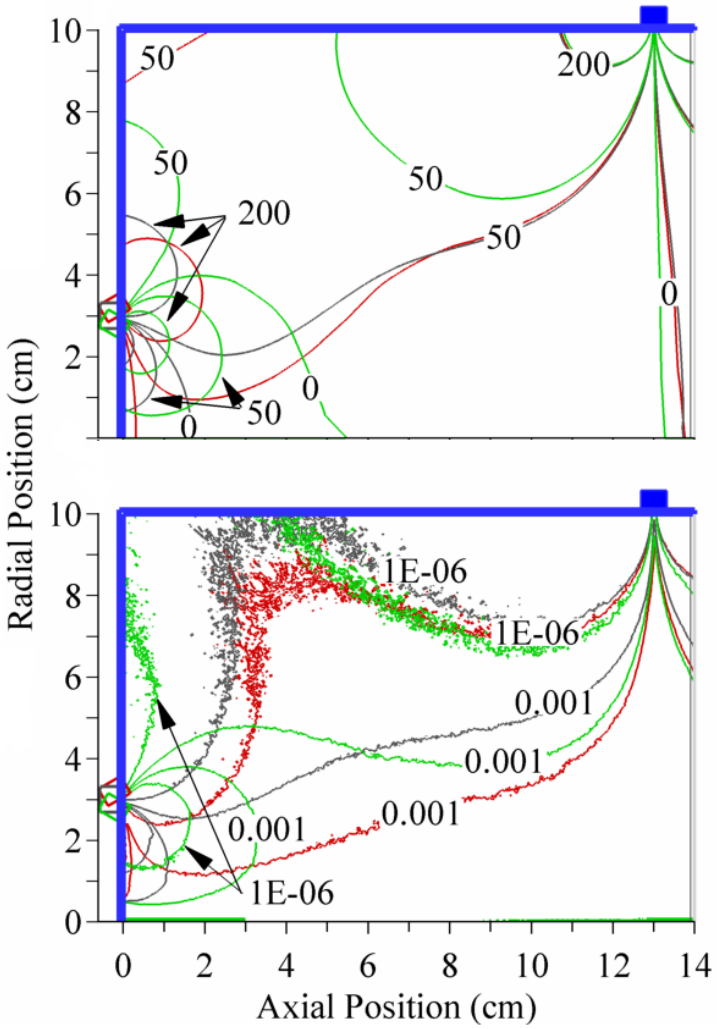

Figure 4.22: Magnetic vector potential contours (in gauss-cm) and relative number density contours for a front-side magnet pair with varying front magnet orientation.

regions wall as strong magnetic field lines, like the $50 gauss\text{-}cm$ line, originate and terminate at its own poles for acute magnet angles. The relative number density plot in Fig. 4.22 shows that the hole at the lower front wall just above the cathode has high concentrations of electrons. Conversely at obtuse angles, although electron absorption at upper front wall and side wall decrease, absorption at the lower front wall steeply increases. The decrease

in electron absorption at the upper front and side wall region occur as strong magnetic field contours like the $50 gauss\text{-}cm$ line originate and terminate at alternate magnets as observed in Fig. 4.22. The presence of the 1×10^{-6} number density contour line indicates that unlike acute orientations, the density of electrons near the upper front and side wall region is less. The decrease in confinement length when a front magnet is oriented at an angle larger than 90° results from the steep increase in electron absorption at the lower front wall. As seen in the magnetic vector potential contour plot in Fig. 4.22, only weak magnetic field lines (like the $0 gauss\text{-}cm$ contour) run closest and parallel to the lower front wall. Hence electrons easily reach this region and there is an increased concentration of electrons as observed in the number density contour plot. In the number density plot, the percentage of electrons in this region is high since the 0.001 contour line is closest to the lower front wall.

In summary, the flux and contour plots indicate that when a magnet's axis of polarization is not parallel to the normal of the wall on which it is located, the introduced weak magnetic field along the walls close to that magnet experience high electron absorption. A 90° magnet orientation provides increased electron confinement by better protecting the wall close to the magnet cusp.

4.2.3 Front-Side Pair with Varying Radial Spacing

For a front-side magnet pair configuration, finding the radial spacing that provides maximum electron confinement is surveyed using the configurations shown in Figs. 3.4 and 3.7. To obtain valid results, both surveys have the front magnet perpendicular to the side magnet and its position is within the $3cm$ to $4cm$ guideline specified in the surveys where the radial

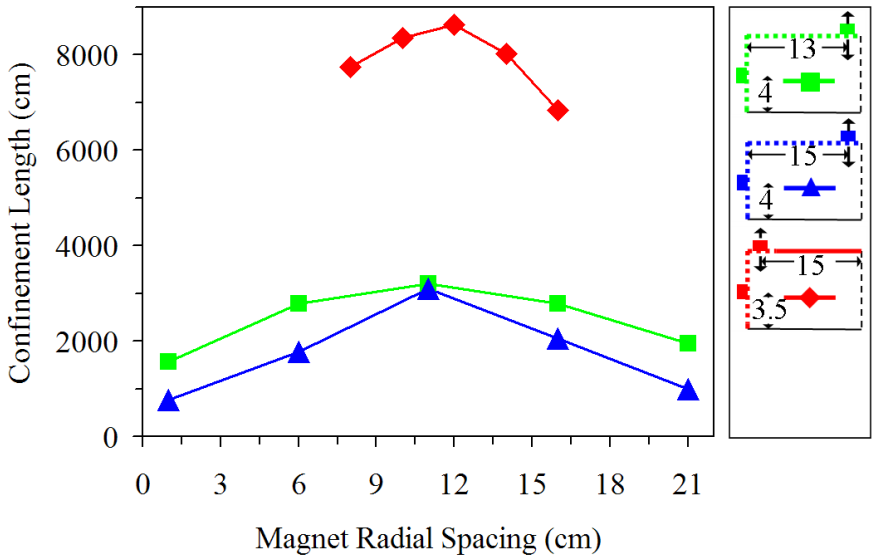

Figure 4.23: Confinement length as a function of the radial spacing between a front-side magnet pair.

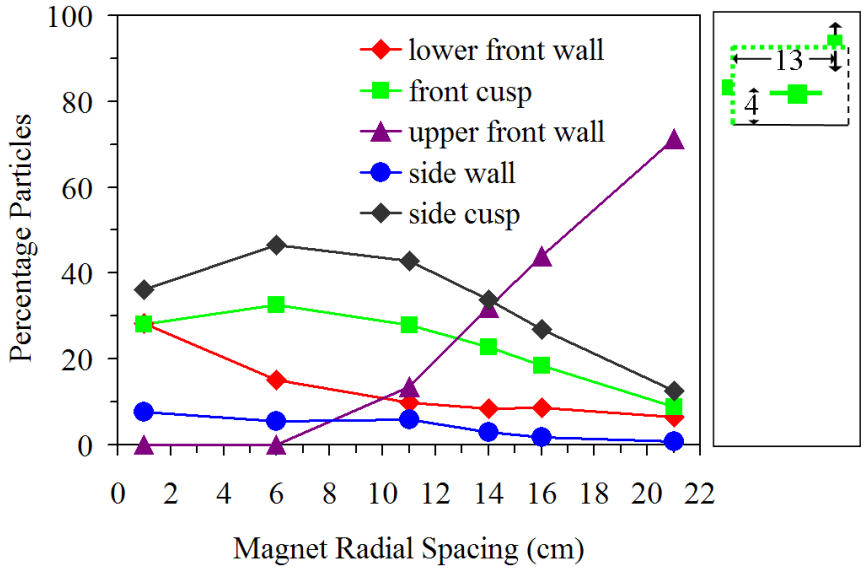

Figure 4.24: Percentage of particles absorbed as a function of the radial spacing between a front-side magnet pair.

position of the front magnet was studied (Sections 4.2.1 and 4.2.4). As shown in Fig. 4.23, when the axial spacing between the magnet pair is fixed at $13cm$ (obtained in Section 4.1.3) or at an arbitrary $15cm$, or $1cm$ from the front wall, the radial spacing that maximizes confinement invariantly occurs between $10cm$ and $12cm$. Although this radial spacing survey and the axial spacing survey of a front-side magnet pair configuration are somewhat similar configurations, the optimal range in this radial spacing survey differs from the optimal $13cm$ axial spacing. This arises from the difference in relative displacements between the magnet pair since the magnet pair axial separation in this radial spacing survey is small compared to the radial separation in the axial spacing survey.

The particle flux plot in Fig. 4.24 illustrates the factors that decrease the confinement length at close and far radial spacings. This plot shows the percentage of particles absorbed at the different regions for an optimized configuration where the magnet pair is spaced at $13cm$ and the front magnet is positioned $4cm$ from the axis. As the radial spacing is altered, the variation in electron confinement primarily results from the changing electron absorption at the upper front wall. At close radial spacings, magnetic field lines at the upper front wall region are strong enough to protect the wall so that electron absorption in this region is minute. At this spacing, higher electron absorptions at the cusps and the lower front wall contribute more to decreasing confinement length. When the radial distance between the magnets increases, the weakening magnetic field in the upper front region means more electrons are absorbed here. For far axial spacings, the decrease in absorption at other regions results from the domination of the absorption at the exposed upper front wall where the hole in the magnetic field allows greater numbers of particles to reach the

wall, thereby consequently decreasing confinement length.

In summary, this survey concludes that optimum primary electron confinement is obtained when the radial spacing between a front-side magnet pair is in the $10cm$ to $12cm$ range. In essence, for large discharge chamber diameters where the radial spacing between the fixed front magnet and the side magnet exceeds $12cm$, an additional magnet ring should be situated at about the chambers upper front corner where high electron absorption occurs. Since the front magnet is $4cm$ from the axis, this corresponds to a chamber whose radius exceeds $16cm$, roughly a $30cm$ diameter chamber. As observed, this guideline on the radial spacing is largely independent of the axial spacing between adjacent magnet rings.

4.2.4 Front-Back Pair with Varying Front-Wall Magnet Radial Position

Like the front-side magnet pair survey in Section 4.2.1, a front-back magnet pair survey (Fig. 3.5) aims to deduce the position of the front magnet that optimizes electron confinement. Based on the guideline deduced from the front-back magnet pair survey presented in Section 4.1.4, the axial spacing between the magnet pair is fixed at $16cm$. As shown in Fig. 4.25, for all chamber radii, maximum confinement occurs when the front magnet lies $3.5cm$ to $5.5cm$ from the chambers' axis. Specifically, the $5cm$ and $10cm$ radii chambers, both provide maximum confinement for the front magnet at $3.5cm$, while the $20cm$ radius chamber provides maximum confinement at $5.5cm$. Irrespective of the slight variation in the exact optimal radial position of the front magnet for all chamber radii, the confinement length decreases at small and large radial positions because of anode biased wall absorp-

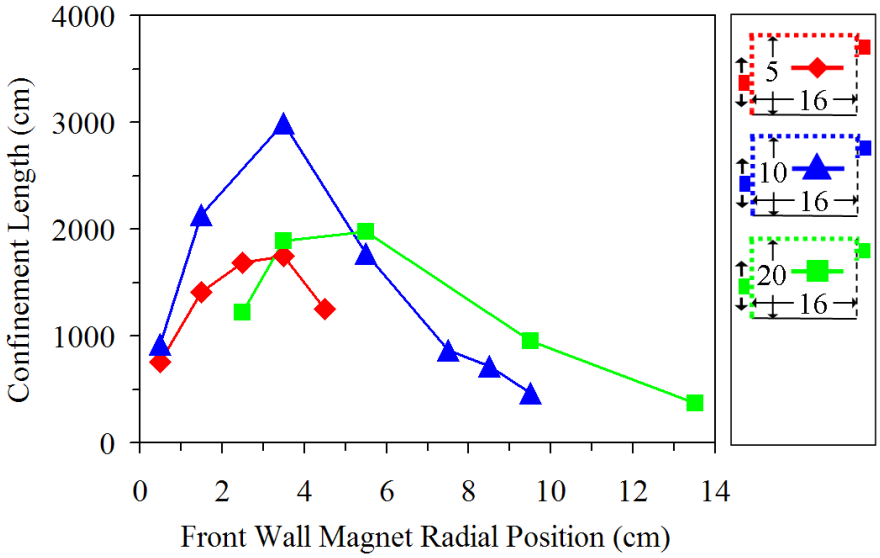

Figure 4.25: Confinement length as a function of the radial position of a front magnet on a front-back magnet pair.

tion. The decrease in confinement, results from the changing electron absorption at the different chamber wall regions. The particle flux plot in Fig. 4.26, illustrates how electron absorbtion at the different wall regions reduce electron confinement. At small and large radial distances of the front magnet, absorption at the cusps does not contribute much to decrease confinement when they are compared to absorption at the walls. At large radial positions, a hole in the magnetic field is introduced at the lower front wall (shown in Fig. 4.27), and as evident in the particle flux plot, electron absorption at the lower front wall is therefore dominant. This magnetic field hole at the lower front wall is always present in a ring-cusp magnet configuration on an axi-symmetric chamber. In the magnetic vector potential plot in Fig. 4.27, this hole results because strong magnetic field lines do not run parallel but perpendicular to the lower front wall. In the number density plot, the intersec-

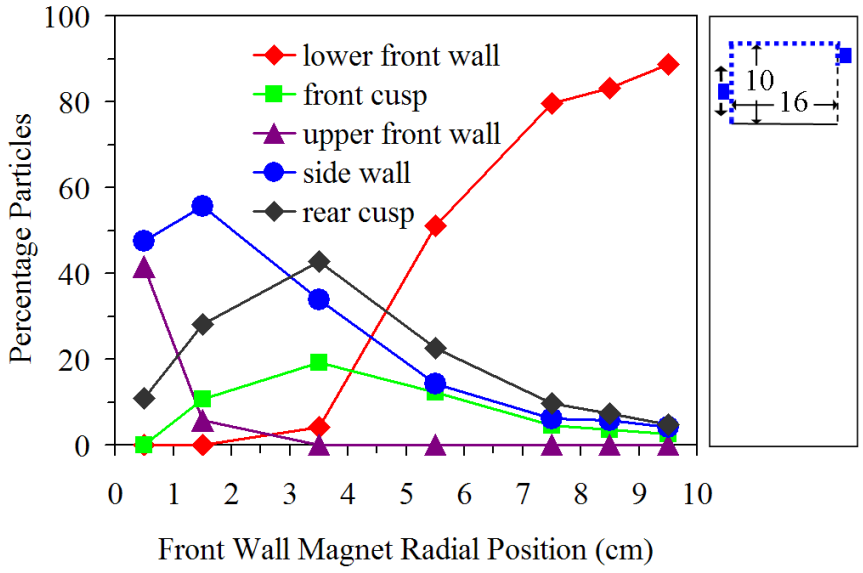

Figure 4.26: Percentage of particles absorbed as a function of the radial position of the front magnet for a front-back magnet pair.

tion of the 1×10^{-6} contour line with the wall, indicates a high number of electrons contact the lower front wall. The sensitivity and occurrence of this hole constrains the distance between the front magnet and the axis. For small radial positions of the front magnet, the lower front wall is adequately protected but the increase in absorption at the upper front wall and side wall regions (Fig. 4.26) results from the weak magnetic field present in these regions (Fig. 4.27). As the front magnet approaches the chamber axis, the separation of the $50 gauss\text{-}cm$ field line illustrates the developing hole is now only occupied by weak field lines. The increase in the number density of the electrons contacting the upper front and side wall, verifies the increase in percentage particle absorption in this region. The optimal placement of the front magnet occurs when there is a balance between the absorption at the lower front wall hole and the absorption at the upper front and side wall. The intersection

of the particle flux line for these regions (Fig. 4.26) indicates a balance that corresponds to the optimal placement of the front magnet ring. Note that this balance has the back magnet much closer to the chamber centerline than the side wall. This is due to the symmetric arrangement of the permanent magnets.

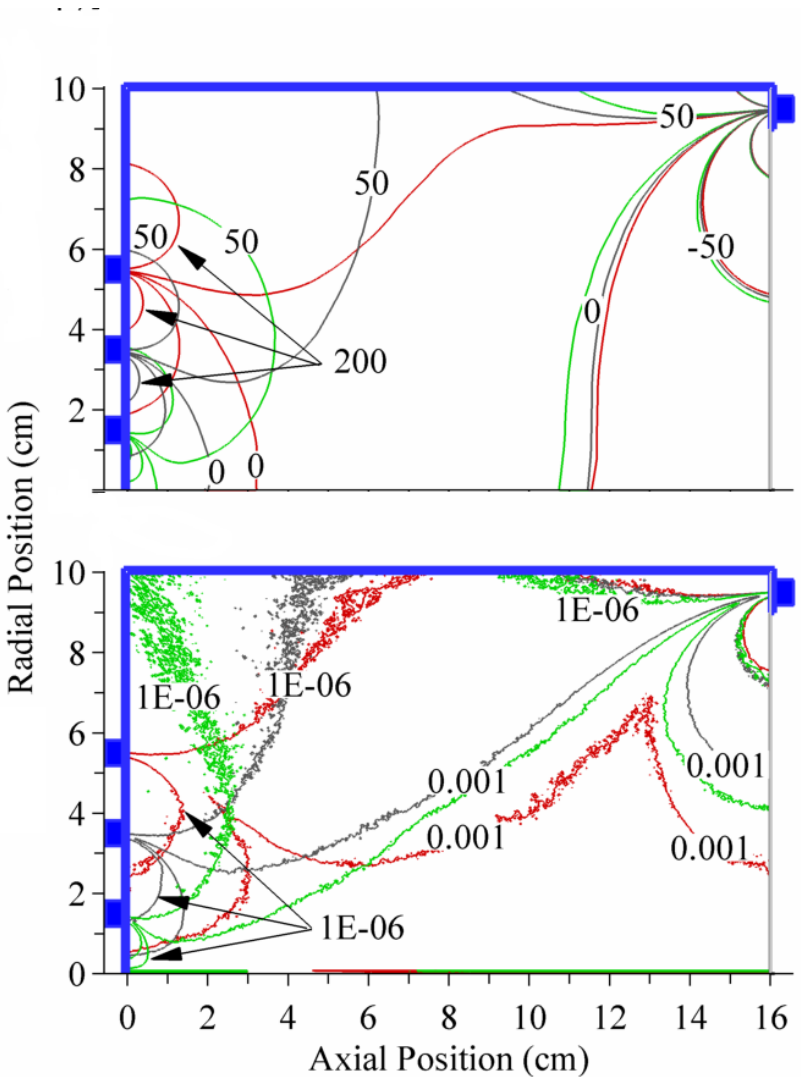

Figure 4.27: Magnetic vector potential contours (in gauss-cm) and relative number density contours for a front-back magnet pair with varying front magnet radial position.

In summary, the front-back magnet pair configuration survey, complements the guide-

line obtained from the survey of the front-side magnet pair where the front magnet radial position is also varied. In the front-side magnet pair survey, maximum confinement was obtained for the front magnet positioned $3cm$ to $4cm$ from the axis. The front-back magnet pair studied herein, validates these results. Since the front-back magnet pair similarly specifies that the front magnet ring should lie $3.5cm$ to $5.5cm$ from the chamber's axis of symmetry, it is conclusive that the placement of a front magnet is independent of the other magnet rings present on the discharge chamber. It should be noted that the developing hole in the upper front and side wall regions can be addressed with a third magnetic ring added to the front-back magnet pair.

4.2.5 Front-Back Pair with Varying Radial Spacing

Like the front-side magnet pair survey (Section 4.2.3) of the radial spacing that provides maximum electron confinement, a front-back magnet pair (Fig. 3.5) survey determines the effect of the radial spacing on confinement. To obtain results that only reflect the radial interaction between the magnet pair, this configuration has the axial spacing between the magnet pair at the $16cm$ based on the results of Section 4.1.4. Furthermore, the high electron absorption at the lower front wall that excessively skews results, is mitigated by positioning the front magnet ring $4cm$ from the axis. As the chamber's radius, and thus the radial spacing between the magnet pair increases, the confinement length increases to a maximum at a magnet position of $11cm$, and then decreases for larger spacings (Fig. 4.28). In other words, maximum confinement occurs when the chambers diameter is $31cm$. For a front-back magnet pair with no radial offset (Section 4.1.4), maximum confinement occurs

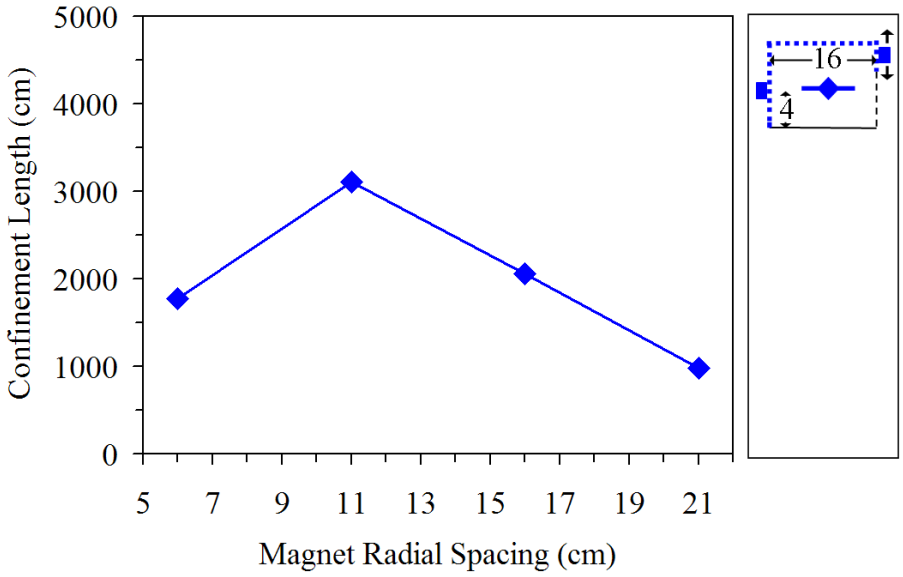

Figure 4.28: Confinement length as a function of the radial spacing between a front-back magnet pair.

at $16cm$. Although, the survey herein provides an optimal radial spacing of $11cm$, the setup of the magnet circuit in this survey gives the actual magnet pair displacement at roughly $16cm$.

The particle absorption plot in Fig. 4.29 illustrates the primary electron loss regions that result in decreasing confinement length when the magnets are placed too close or far apart. Electron absorptions at the upper and lower front wall dictate the trend seen in the confinement length. At close spacings, the upper front wall and the side walls are adequately shielded by strong magnet field lines running between magnets and parallel to this region. Hence electron absorption at this region is minimal thereby resulting in the subsequently high absorption at the lower front wall. For large magnet radial spacings, absorption at the upper front wall dominates the other regions, since weak magnet field

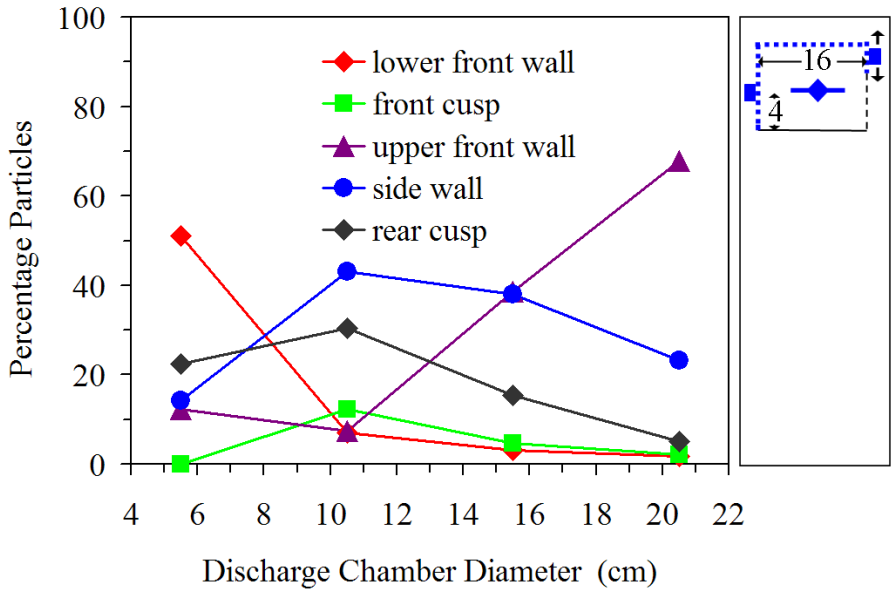

Figure 4.29: Percentage of particles absorbed as a function of the radial spacing between a front-back magnet pair.

lines leave holes here.

In summary, this survey concludes that optimum primary electron confinement occurs when the radial spacing between a front-back magnet pair is about $11cm$. The validity of this guideline is seen in a similar front-side magnet pair survey which prescribes the range at $10cm$ to $12cm$. For large discharge chamber diameters where the radial spacing between the fixed front magnet and the back magnet exceeds $11cm$, the diameter exceeds $30cm$, an additional magnet ring should be situated around the upper front corner of the discharge chamber.

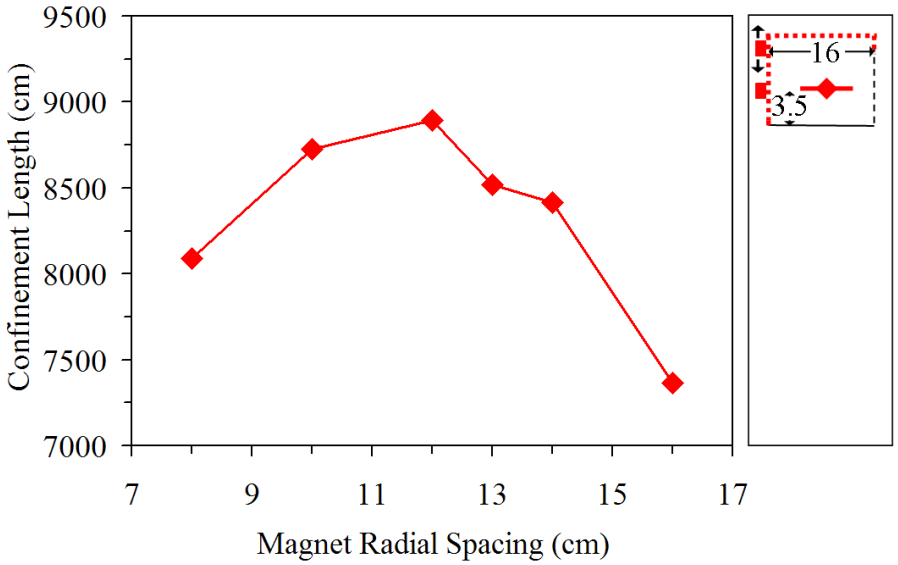

Figure 4.30: Confinement length as a function of the radial spacing position between a front-front magnet pair.

4.2.6 Front-Front Pair with Varying Radial Spacing

Similar to the side-side magnet pair survey in Section 4.1.2, a front-front magnet pair survey aims to determine the radial spacing that provides maximum electron confinement in a discharge chamber. The schematics for this configuration pair, shown in Fig. 3.8, have the radial spacing varied by the diameter of the chamber. To isolate the radial interaction between the magnet pair, the unprotected side wall is set to reflect electrons. Furthermore, isolating their radial interaction requires mitigating electron absorption at the unprotected lower front wall which is highly sensitive to electron absorption. This sensitivity is seen in the surveys where the front magnet radial position varies (Sections 4.2.1 and 4.2.4) and the unprotected lower front wall dominates other electron absorbtion sites, thereby significantly shortening confinement lengths. To prevent this, it is recommended that the

lower front magnets radial position be $3.5cm$. The front-front magnet pair survey provides maximum confinement when the radial spacing is $12cm$ (Fig. 4.30).

The factors that produce low confinement lengths for small and large radial spacings are similarly responsible for the decrease in confinement in the side-side magnet pair survey. At close magnet spacings, the cusps are the primary electron absorption sites. When the magnets are spaced too far apart, the magnetic field lines at an intermediate distance between the pair are weak. The magnetic vector potential plot in Fig. 4.31 show the existing hole. As the magnetic field hole permits electrons to easily reach the chamber wall, electron confinement decreases as electrons are increasingly absorbed at the front wall. In the number density plots in Fig. 4.31, the front wall increasingly intersects the 1×10^{-6} contour line as the chamber's radius increases. This indicates that a high percentage of electrons contact the front wall, hence the decrease in confinement.

In conclusion, a spacing guideline for this survey is slightly identical to the results obtained in the similar side-side magnet pair survey. Adjacent magnets on the same wall should be spaced no greater than $12cm$ apart.

4.3 Summary of Survey Results

All the configurations discussed are summarized in this section. To summarize and aid comparison between magnet circuit configurations, survey results obtained from the previous sections are tabulated in Table 4.1. As discussed earlier, all configurations are grouped into classes depending on if either the axial or radial spacing or position is varied. The

convention for the configurations studied, is based on the walls on which the magnet rings are situated. Since the deduced guidelines for each survey result is to be used as a starting point for magnet circuit design for a discharge chamber, precision is not necessary. Thus range values describing the guidelines are sufficient.

Class	Pair Location	Variable	Orientation	Survey Results
Axial	Side Wall	Number of Side Wall Magnet Rings	180° †	$9cm$ – $18cm$
	Side-Side	Axial Spacing	180° †	$12cm$ – $15cm$
	Front-Side	Front Wall Magnet Orientation and Axial Spacing	90° ‡, 120°, 150°	$13cm$
	Front-Back	Axial Spacing	0°	$11cm$ – $16cm$
	Side-Back	Axial Spacing	90°	$14cm$ – $15cm$
Radial	Front-Side	Front Wall Magnet Orientation and Radial Position	90° ‡, 120°, 150°	$3cm$ – $4cm$
	Front-Side	Front Wall Magnet Orientation Only	30°, 60°, 90°, 120°, 150°	90°
	Front-Side	Radial Spacing	90°	$10cm$ – $12cm$
	Front-Back	Front Wall Magnet Radial Position	0°	$3.5cm$ – $5.5cm$
	Front-Back	Radial Spacing	0°	$11cm$
	Front-Front	Radial Spacing	180°	$12cm$

† survey performed by Deshpande and Menart (2004) ‡ survey performed by Deshpande et al. (2005)

Table 4.1: Ring-cusp magnet circuit configuration results.

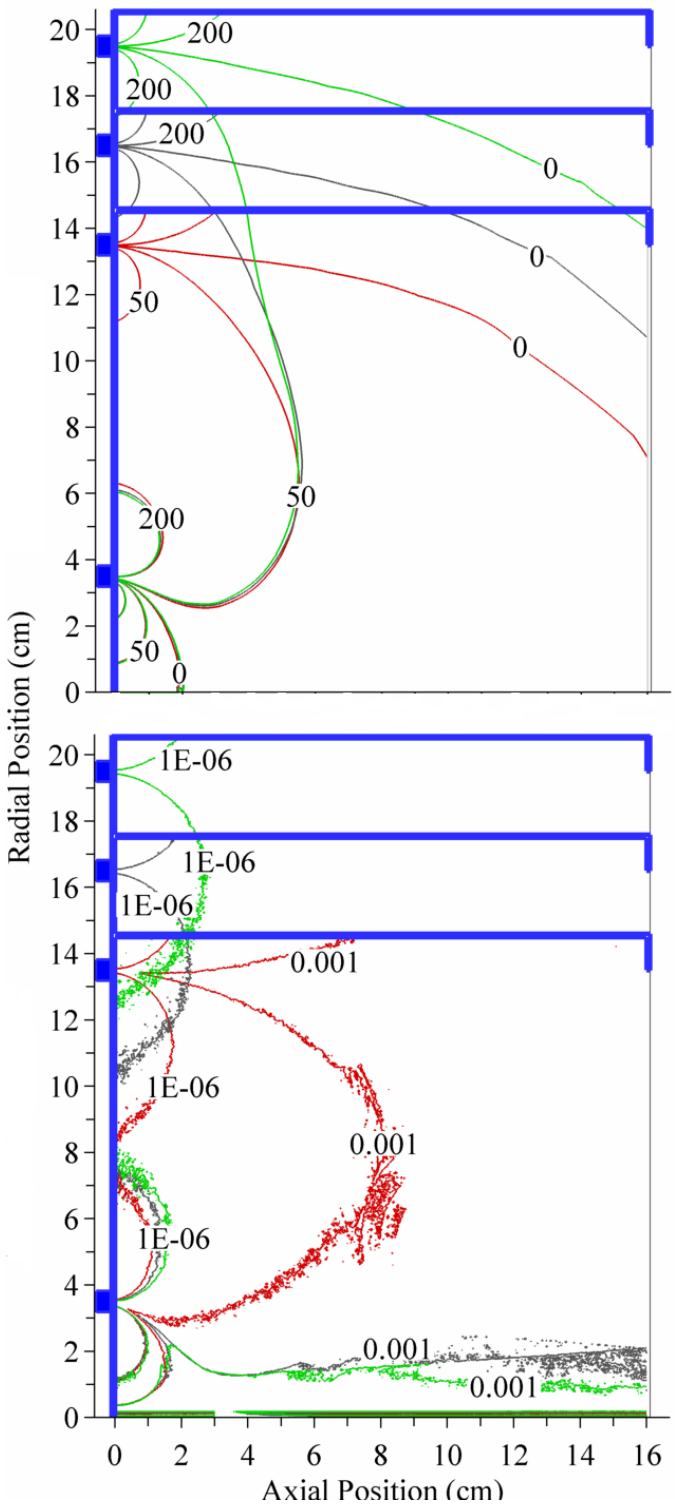

Figure 4.31: Magnetic vector potential contours (in gauss-cm) and relative number density contours for a front-front magnet pair with varying radial spacing.

5. Complex Magnet Circuit Configurations

The optimal location, position, and orientation of the magnet rings that comprise the magnet circuit on a discharge chamber are surveyed in Chapter 3, and the results are presented in Chapter 4. The surveys, summarized in Table 4.1, focuses on the axial and radial interaction between magnet pairs situated on the front, side, or back walls of the chamber. Since the results of the magnet pair configurations surveyed occasionally show that additional magnet rings are necessary to provide adequate electron confinement in large chambers, this chapter proceeds to survey a magnet circuit with three magnet rings. To optimize primary electron confinement, the combination of the three magnet rings are based on the guidelines deduced from the magnet pair surveys. To test the validity of the guidelines used, a comparison is made between the confinement length of the optimized magnet circuit and a similar circuit that includes a slight deviation from the optimized circuit. The results of the comparison (tabulated in Table 5.1) invariantly show that the non-optimized magnet circuit decreases the electron confinement length; thereby certifying the general guidelines obtained in all surveys in the previous chapter.

5.1 Test of Guidelines on a Magnet Circuit with Three Magnet Rings

A survey of a magnet circuit with more than two magnets aims to validate the guideline which establishes the benefit or advantage of an additional magnet. First, the optimal radial spacing between the front-side and front-back magnet pair configurations (presented in Chapter 4 Sections 4.2.3 and 4.2.4 respectively), shows that a chamber radius larger than $16cm$ requires an additional magnet ring. In both surveys the lower confinement lengths that occur for very large radii chambers, result from high particle absorption at the upper front wall region where there exists a magnetic field hole (Figs. 4.24 and 4.29). In these surveys, it should be noted that the front magnet is only a short distance from the axis to avoid the dominant high electron absorptions that would otherwise occur at the lower front wall region. The weak magnetic field lines at the upper front wall can be stemmed by situating a magnet ring in that vicinity. In the fixed length chamber study presented in Chapter 4 Section 4.1.1, Deshpande et al. (2005) concluded that increasing the number of magnet rings can lower the confinement ability of a chamber since more cusps provide more locations where electrons can be absorbed. Thus, though the introduction of an additional magnet ring may stem absorbtion at the upper front wall, it conversely enhances electron absorption at the additional cusp. The competing electron absorption at the upper front wall and at the additional cusp is illustrated in the confinement length plot in Fig. 5.1. For the front-side and front-back magnet pair surveys, the front magnet position and the axial and radial spacing between the pair are based on guideline values from the surveys

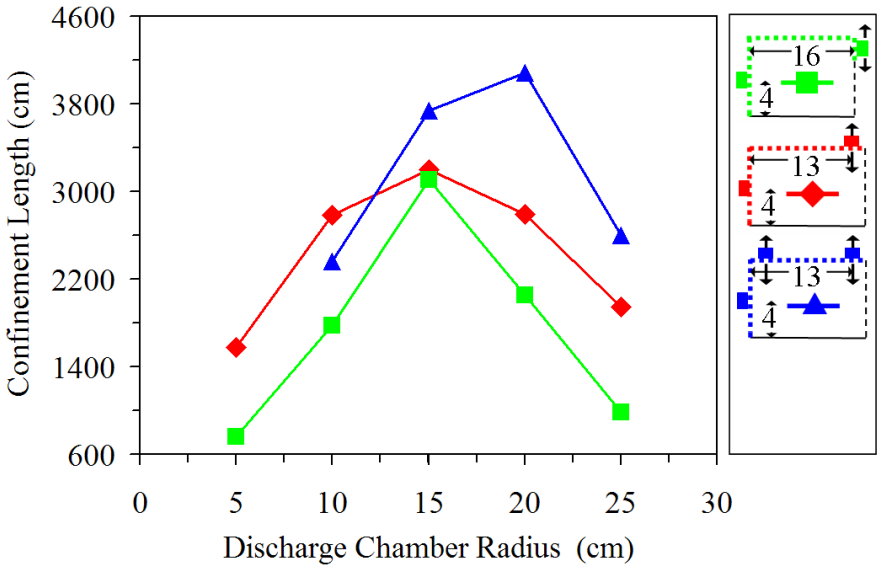

Figure 5.1: Confinement length as a function of the radial spacing between a front-back, front-side magnet pair.

in the previous chapter. The front-side-side magnet ring survey introduces to the front-side magnet pair configuration an additional side magnet situated $1cm$ from the front wall of the chamber. In all three surveys, the radial spacing varies with the chamber's radius. The intersection of the front-side and the front-side-side magnet configuration plots in Fig. 5.1, indicate the benefit of increased electron confinement with three magnet rings occurs when the discharge chamber radius is larger than a radius of $13cm$. For chamber radii less than $13cm$ a third magnet ring is detrimental, since the confinement length is lower than those obtained for a similar configuration with only two magnet rings. It should be noted that this guideline is specific to this configuration.

Three magnet rings on a $20cm$ radius chamber are used to test the validity of the guidelines deduced in Chapter 4. In the three magnet circuit configuration surveys, the

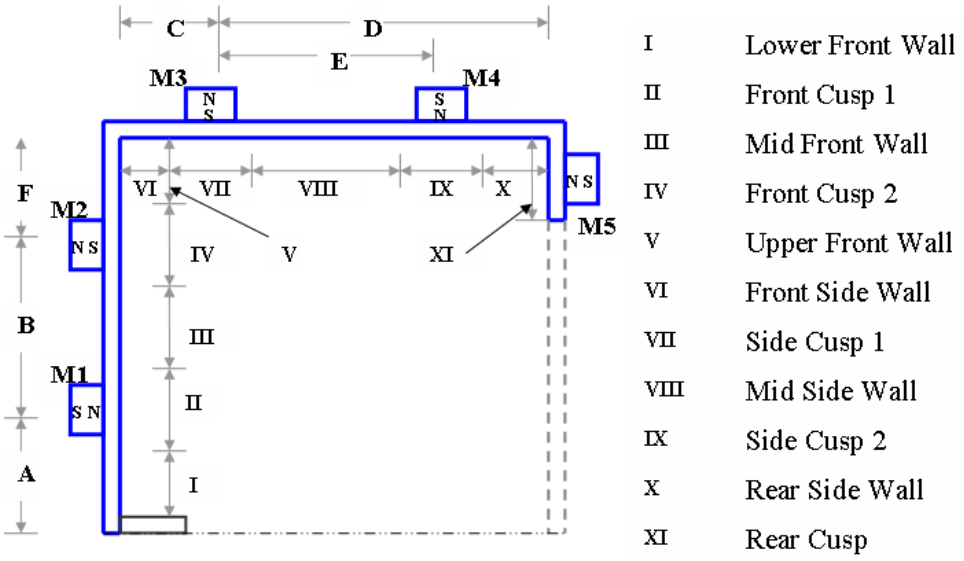

Figure 5.2: Guideline test on complex magnet configurations with three magnet rings. For each three ring magnet circuit, two of the magnet rings are removed.

three magnet rings on the $18cm$ long chamber are arranged with the guidelines applicable only to adjacent magnet rings. The first validation survey has a magnet circuit with a front ($M1$), side ($M3$), and rear ($M5$) magnet (Fig. 5.2). For this $M1$, $M3$, and $M5$ magnet circuit configuration, a first case run is labeled case $1a$. For an alternate case run (case $1b$), the magnet configuration still includes magnets $M1$, $M3$ and $M5$, but the positions are slightly altered to those used in case $1a$. In a second validation survey, a front magnet ($M1$) and two side magnets ($M3$ and $M4$) are used. The first case with this magnet configuration is called case $2c$ and it utilizes two guidelines between adjacent magnet rings. An alternate case run (case $2d$) with magnets $M1$, $M3$, and $M4$, introduces a slight alteration to the case $2c$. The last validation survey has two front magnet rings and one side magnet ring. This configuration corresponds to magnets $M1$, $M2$ and $M3$.

Cases $3e$ and $3f$ are used in this configuration where $3e$ obeys the guidelines and $3f$ has some slight magnet circuit alterations from the guidelines. All validation surveys and their results are listed in Table 5.1.

$M1$, $M3$, $M5$ Configuration: Cases $1a$ and $1b$

The spacing and position of the magnets in this circuit is given in Table 5.1. Case $1a$ has A, the front magnet ($M1$) distance from the chambers axis at $4cm$. This is within the guideline for the radial position for a front magnet. The $15cm$ axial distance D between magnets $M3$ and $M5$ is within the $11cm$–$16cm$ guideline. The back magnet ring is centered on a $1cm$ lip. The radial spacing between magnets $M1$ and $M3$ is $16cm$; slightly bigger than the established $10cm$–$12cm$ guideline spacing. The confinement length for case $1a$ is $4383cm$. The two magnet position alterations made to case $1a$ that give case $1b$ are the radial position of the front magnet ring is moved to $6cm$ (this is $2cm$ bigger than recommended), and the separation between the side magnet and the back magnet, is increased to $17cm$. Consequently, the confinement length for case $1b$ is $2895cm$. The fact that confinement length of case $1b$ is considerably less than the confinement length of case $1a$ provides some validation of the guidelines stated in this paper. The increased radial position of front magnet and the large axial spacing between the side and back magnets contribute to the reduction in confinement length since the lower front wall (region I) and the side wall (region VIII, IX, X) are now exposed. Hence there is the increase in the percentage of electrons absorbed at these regions (listed in Table 5.1). Most significantly, the highly increased absorption at the lower front wall (from 3.8% to 36.0%) validates the guideline for the positioning of the

Case	Magnets	Circuit Configuration (cm)						% of Particles Absorbed at Cusp and Wall Regions											Conf.
		A	B	C	D	E	F	I	II	III	IV	V	VI	VII	VIII	IX	X	XI	Length
1a	$M1$, $M3$, $M5$	4^*	–	3	15^*	–	–	3.8	9.7	←	25.8	→	0.0	18.2	←	15.9	→	26.5	4383
1b	$M1$, $M3$, $M5$	6	–	1	17	–	–	36.0	6.2	←	12.5	→	0.0	11.8	←	17.8	→	15.7	2895
2c	$M1$, $M3$, $M4$	4^*	–	5	13	12^*	–	4.2	9.4	←	28.5	→	0.0	29.1	2.3	26.6	0.0	–	5555
2d	$M1$, $M3$, $M4$	2	–	3	15	14^*	–	0.1	3.8	←	61.3	→	0.0	15.2	3.2	16.4	0.0	–	3202
3e	$M1$, $M2$, $M3$	4^*	15^*	14^*	4	–	1	3.7	12.8	17.8	23.1	0.0	12.3	29.7	←	0.6	→	–	4916
3f	$M1$, $M2$, $M3$	4^*	15^*	17	1	–	1	3.2	11.4	16.1	26.6	0.0	16.6	26.0	←	0.0	→	–	5067

$*$ value within guidelines $\leftarrow \# \rightarrow$ number spans regions For case $3f$ the upper front magnet $M2$ is oriented at $120°$.

Table 5.1: Maximum confinement results for three magnet circuit configurations, each with three magnet rings on a $40cm$ diameter, $18cm$ long discharge chamber.

front magnet relative to the chamber's centerline.

$M1$, $M3$, and $M4$ Configuration: Cases $2c$ and $2d$

The configuration and results from the study of the magnet circuit with magnets $M1$, $M3$, and $M4$, are shown in Table 5.1. Case $2c$ utilizes the guidelines from Chapter 4, and case $2d$ slightly violates the guidelines. Case $2c$ has the front magnet ($M1$), located $4cm$ from the chamber's axis, and the axial spacing between the parallel side magnets ($M3$ and $M4$) is $12cm$. This axial spacing lies within the specified $12cm$–$15cm$ range. Since the rear side magnet ($M4$) is $1cm$ from the rear of the chamber, this leaves the front side magnet ($M3$), $5cm$ from the front wall (distance C). For case $2d$, the alterations made to the configuration of case $2c$ include a decrease in the radial distance of the front magnet from the axis ($2cm$), and a decrease in C so that magnet $M3$ is spaced $15cm$ from magnet $M4$ which remains positioned $1cm$ from the rear of the chamber. The $15cm$ spacing is still within the $14cm$–$15cm$ guideline for a side-back magnet pair. For case $2c$ the confinement length is $5555cm$, and the for case $2d$ it is $3202cm$. The results for this survey validate the applied guidelines. The primary reason for the decreased confinement ability for the magnet circuit for case $2d$ is the $18cm$ radial separation between magnets $M1$ and $M3$. For a front-side magnet pair survey where the radial spacing was varied, the favorable spacing was $10cm$–$12cm$, hence at $18cm$ there is an increase in electrons absorbed at the upper front wall (regions III, IV and V). The percentage of particles absorbed at this region increases from 28.5% in case $2c$ to 61.3% in case $2d$. It should be noted that cases $1a$ and $2c$ both satisfy the guidelines laid out in this work, but case $2c$ has the longer confinement length. The reason for the

differences is that the lip region in case $1a$ is not present in case $2c$. If a lip region were added to case $2c$ its confinement length would decrease. At the present time no guidelines to why case $2c$ is better than $1a$ can be stated.

$M1$, $M2$, $M3$ Configuration: Case $3e$ and $3f$

This validation survey has magnets $M1$, $M2$ and $M3$ (shown in Fig. 5.2) configured such that case $3e$ utilizes some guidelines from Chapter 4. The radial spacing B between the front magnet rings ($M1$ and $M2$) is at $15cm$ which is slightly larger that the $12cm$ guideline for front-front magnet pairs. The distance A, is optimized at $4cm$, and C is also within guidelines at $14cm$. The confinement length for this case is $4916cm$. The alteration to this case involves increasing the spacing between the upper front magnet and the side magnets by positioning the side magnet ($M3$) $1cm$ from the back wall of the chamber. At $17cm$, the axial spacing now lies outside the $13cm$ axial spacing guideline for a front-side wall magnet pair. Another alteration rotates the lower front magnet ($M2$) so it is oriented at $120°$ to the pole of the side magnet. This is an adverse alteration since a guideline states that maximum confinement lengths are obtained when the pole of the magnet is parallel to the normal of the surface. Although it is expected that these two deviations from the guidelines would result in a decrease in the confinement ability of the chamber when compared to case $3e$, the two confinement lengths are approximately equal. Case $3f$ confinement length is $5067cm$, while case $3e$'s confinement length is $4916cm$. For these two cases no large changes in the electron absorption at any wall or cusp region occur. Although, there should be an increase in absorption at the upper front wall since C increases. The unrealized effect

validates the slight independence between axial and radial spacings. In this survey, the radial spacing between the front and front side magnets provides adequate wall protection even for a slight shift in the axial spacing. Also, another possibility for the difference in these two cases is the amount of wall area exposed between the magnet side magnet and the back wall. There is $4cm$ of side wall to the outside of $M3$. For all the studies did in this paper the outside wall areas on the magnets was kept below $1cm$. It is believed that this distance can be extended to $2cm$ or $3cm$, but not to $4cm$.

6. Conclusions and Future Work

In summary, various ring-cusp magnet pair configurations were computationally studied and guidelines on the spacing, position, and orientation of samarium cobalt magnets that comprised a magnet circuit on an axi-symmetric discharge chamber were deduced. So that the guidelines obtained from these surveys are not skewed, the walls of the chamber were chosen to be aluminum and do not interact with the magnetic fields. The work here builds on initial surveys performed by Deshpande and Menart (2004) and Deshpande et al. (2005). All magnet circuit configuration surveys presented here are listed in Table 3.1 (page 32) and the corresponding guidelines deduced are listed in Table 4.1 (page 85).

This work simply looks at the ability of a magnet circuit to confine electrons in the discharge chamber. Other important factors in magnet circuit design are how the magnetic field affects the location of ions, and how the magnetic field affects the stable operation of the plasma discharge. In addition to these factors, there are a number of unstudied parameters that can influence how a given magnetic field confines electrons. For these reasons, a caveat is that the guidelines stated here should not be used as the sole magnet circuit design criteria. Its significance is that it serves as a starting point for magnet circuit designs. Given the complexities involved in the design of a magnet circuit for an ion engine, having a reasonable starting point is very helpful. Since the guidelines given in this paper

are intended to be used as a starting point for magnet circuit design for a discharge chamber, a high degree of precision in the spacing values is not required, nor can it be given based on the limitations of the analysis. Thus stating these guidelines as range of values is beneficial.

All the guidelines for a ring-cusp magnet configuration can be reduced to five simple rules-of-thumb:

1. One magnet ring must be located on the front wall and its radius must be no greater than $4cm$. This guideline is independent of the position or number of magnet rings used on the discharge chamber, but is a function of the diameter of the cathode used.

2. The axial or radial spacing between magnet rings should be between $11cm$ and $16cm$. For a small chamber that does not permit magnet ring spacings this large, two magnetic rings should be used. Conversely, if the discharge chamber is large such that spacings between magnets exceeds $16cm$, an extra magnet ring should be used. If adding an extra magnet ring causes the spacing between adjacent magnet rings to be smaller than the recommended range floor value, another magnet ring should be added. Closer magnet spacings with more magnets are preferred to larger spacings with fewer magnets. In essence, use the fewest magnet rings possible without going outside the recommended spacing range.

3. A corollary to the previous guideline is that for chamber diameters greater than $25cm$, three or more magnet rings should be used to obtain adequate electron confinement. Again, the fewest magnet rings possible should be used.

4. Magnets should be orientated such that their axis of polarization is parallel to the

normal of the wall on which they are positioned.

5. Another guideline that has to be added to this list is a recommendation on the length of the absorbing wall located on the outside of the outer magnet used in a given configuration. From the cusp study work of Deshpande et al.(2004) it would seem that this should be smaller than $2cm$; $1cm$ would be a conservative value to use. More investigation into this number is required.

At the present time only primary electrons are computationally analyzed using PRIMA. A comparison study to experimental results has provided confidence about the accuracy of the results produced by PRIMA. At the time of this work, Mahalingam (2006) is presently continuing Ph.D work on the development of XOOPIC, a computer model that tracks ions, secondary electrons, and neutral particles, as well as primary electrons. This work is in progress at Wright State university at the moment. Future work will study the spacing and position of the magnets on an actual conical-cylindrical discharge chamber model. Also, the effect of the cathode position on confinement would be studied in the future using PRIMA. A future study will also have to address the effect of a discharge chamber's aspect ratio on electron confinement.

7. References

Arakawa, Y. and Wilbur, P.," Discharge chamber calculations in cusped ion thrusters using the finite element method," Proceedings of International Electrical Propulsion Conference paper, pp. 460-466 AIAA-88-079, 1988.

Arakawa, Y. and Yamada, T., "Monte Carlo simulations of primary electron motions in cusped discharge chambers," International Electrical Propulsion Conference paper AIAA-90-2654, 1990.

Arakawa, Y. and Ishihara, K., "A numerical code for cusped ion thrusters," International Electrical Propulsion conference paper IEPC-91-118, 1991.

Arakawa, Y. and Wilbur, P. J., "Finite element analysis of plasma flows in cusped discharge chambers," *Journal of Propulsion and Power*, Vol.7, pp. 125 - 128, 1991.

Brophy, J. R. and Wilbur, P. J., "Simple performance model for ring and line cusp ion thruster," *AIAA Journal*, Vol. 23, pp. 1731 - 1736, 1985.

Beer, P. and Johnston, E., *Vector Mechanics for Engineers*, 5^{th} edition, McGraw-Hill, 1988.

Brophy, J.,"A detailed model of ion propulsion systems,"25th AIAA/ASME/SAE/ASEE, Joint Propulsion Conference paper AIAA 89-2268, 1989.

Beattie, J. R. and Matossian, J. N., "Inert-gas ion thruster technology," NASA contract report, Contract no. NAS 3-23860, 1992.

Bronson, G. and Walter, K., *Modern FORTRAN 77/90/2000*, 3^{rd} edition, Scott Jones, 1999.

Choueiri, E.Y., "A Critical History of Electric Propulsion: The First 50 Years (1906-1956)," Journal of Propulsion and Power, Vol. 20, No. 2, March-April, 2004.

Deshpande, S., and Menart, J., "Computational Simulations of the Trajectory of Primary Electrons inside the Discharge Chamber of an ion engine," Master Thesis, Wright State University, 2004.

Deshpande, S. et al., "Computational Study of Magnet Placement on the Discharge Chamber of an Ion Engine," 41st AIAA/ASME/SAE/ASEE, Joint Propulsion Conference paper AIAA 05-4254, 2005.

Engel, A., *Electric Plasmas: Their Nature and Uses*, 1^{rd} edition, Taylor and Fracis Inc., 1983.

Fearn, D. B., "The UK-10 ion propulsion system status and applications ," Intelsta Symposium, 1989.

Greenwood, D. T., *Classical Dynamics*, Prentice-Hall, Englewood cliffs, NJ, 1997.

Griffiths, D. J., *Introduction to Electrodynamics*, 2^{nd} edition, Prentice-Hall, Englewood cliffs, NJ, 1989.

Goodchild, M.F., and K.K. Kemp, eds. (NCGIA Core Curriculum in GIS), National Center for Geographic Information and Analysis, University of California, Santa Barbara CA., 1990.

Goosens, M. et al., *The Latex Companion*, Addison, 1994.

Hiatt, J. M. and Wilbur, P. J., "Ring cusp discharge chamber performance optimization," *Journal of Spacecraft and Rockets*, Vol.2, pp 390 - 397, 1986.

Hiatt, J. M. and Wilbur, P. J., "Ring cusp discharge chamber performance optimization," International Electric Propulsion Conference paper IEPC-85-2007, 1985.

Hirakawa, M. and Arakawa, Y., "Plasma particle simulation in cusped ion thrusters," International Electrical Propulsion Conference paper IEPC-93-242, 1993.

Hibbler, R. C., *Engineering Mechanics-Dynamics*, 7^{th} edition, Prentice-Hall, 1995.

Jet Propulsion Laboratory picture archive, http://www.jpl.nasa.gov/pictures/solar/ds1ion.html, 2000.

Joglekar, A., "Magnetic field and primary electron modeling for the discharge chamber of an ion engine," Masters thesis, Wright State University, 2001.

Kauzmann, W. *Kinetic Theory of Gases*, Benjamin, Inc., 1966.

Kopka, H. and Daly, P. W., *A Guide to Latex*, 2^{nd} edition, Addison-Wesley, 1995.

Leung, K. N.," Plasma confinement by localized cusps," *Journal of Physics of Fluid* Vol. 19, pp. 1045-1053, 1976.

Loeb, H. W. et al.,"State-of-the-art of the RIT ion thrusters and their spin-offs," 39^{th} Congress of the International Astronautical Federation paper IAF-88-258, 1988.

Massey, H. S. W. et al., *Electronic and Ionic Impact Phenomena, Vol.1* , 2^{nd} edition, Oxford Press, 1969.

Marcus, A., "Two-Dimensional simulation of cusp confinement of a plasma," *Journal of Plasma Physics* Vol. 22, pp. 1015-1027, 1980.

MAXWELL 2D Website, http://www.ansoft.com, 2004.

Menart, J. A., "Development of a small ion thruster," 1997 NASA-ASEE Summer Faculty Fellowship Program at Lewis Research Center Final Report, pp. 75 - 77, 1997.

Menart, J. A., "Magnetic field codes", NASA internal memo August 13, 1998.

Menart, J. A. and Patterson, M. J., "Magnetic circuit for enhanced discharge chamber performance of a small ion thruster," 34th AIAA/ASME/SAE/ASEE, Joint Propulsion Conference paper AIAA 98-3343, 1998.

Mahalingam, S., and Menart, J., "Primary electron modeling in the discharge chamber of an ion engine," Jet Propulsion Conference paper, AIAA-2002-4262, 2002.

Mahalingam, S., and Menart, J., "Primary electron modeling in the discharge chamber of an ion engine," Master Thesis, Wright State University, 2002.

Mahalingam, S., and Menart, J., Private Communication, 2004.

NASA Deep Space 1 website, http://nmp.jpl.nasa.gov/ds1, 2002.

Rapp, D. and Englander-Golden, P., "Total cross sections for ionization and attachment in gases by electron impact," *Journal of Chemical Physics*, Vol. 43, pp 1464 - 1479, 1965.

Ogunjobi, T. A., "PRIMA: User Manual", Operation manual December 23, 2005.

Ogunjobi, T. A., and Menart, J., "Computational Study of Ring-Cusp Magnet Configurations that Provide Maximum Electron Confinement," 42st AIAA/ASME/SAE/ASEE, Joint Propulsion Conference paper AIAA 05-4254, 2006.

Press, W. H., et al., *Numerical Recipes in Fortran 77*, Vol.1, 1992.

Patterson, M., and Haag, T., "Performance of NASA 30 cm ion thruster," International Electric Propulsion Conference paper, IEPC-93-108, 1993.

Rao, S. S., *The Finite Element Method in Engineering*, 3^{rd} edition, Butterworth-Heinemann, 1999.

Sandonato, G. M. et al., "Magnetic confinement studies for performance enhancement of a 5-cm ion thruster," *IEEE Transactions on Plasma Science*, Vol. 24, No. 6, 1996.

Segerlind, L. J., *Applied Finite Element Analysis*, 2^{nd}edition, John Wiley and Sons, 1984.

Stueber, T., "Discharge chamber primary electron modeling activities in 3-dimension," Jet Propulsion Conference paper, AIAA-2004-4105, 2004.

Wilbur, P. J., "Advanced Ion thruster research report, NASA Contractor report," NASA CR-174862, 1985.

Wilbur, P. J., et al., "Approach to the parametric design of ion thrusters," *Journal of Propulsion and Power*, Vol. 6, pp. 575-583, 1990.

Wirz, R., " A preliminary 2-D computational model of an ion thruster discharge chamber," 39th AIAA/ASME/SAE/ASEE, Joint Propulsion Conference paper, AIAA-2003-5163, 2003.

Wirz, R., and Katz, I., " 2-D discharge chamber model for ion thruster," 41th AIAA/ASME/SAE/ASEE, Joint Propulsion Conference paper, AIAA-2005-3690, 2005.

Yoshida, H. et al., “Performance characteristics of 35-cm diameter xenon ion thruster,” 34th AIAA/ASME/SAE/ASEE, Joint Propulsion Conference paper AIAA 96-2714, 1996.